ISSN 1063-7737, Astronomy Letters, 2018, Vol. 44, No. 6, pp. 390–410. © Pleiades Publishing, Inc., 2018.
Original Russian Text © P.S. Medvedev, I.I. Khabibullin, S.Yu. Sazonov, E.M. Churazov, S.S. Tsygankov, 2018, published in Pis'ma v Astronomicheskii Zhurnal, 2018, Vol. 44, No. 6, pp. 426–449.

An Upper Limit on Nickel Overabundance in the Supercritical Accretion Disk Wind of SS 433 from X-ray Spectroscopy

P. S. Medvedev[1*], I. I. Khabibullin[1,2], S. Yu. Sazonov[1], E. M. Churazov[1,2], and S. S. Tsygankov[1,3]

[1] *Space Research Institute, ul. Profsoyuznaya 84/32, Moscow, 117997 Russia*
[2] *Max Planck Institut für Astrophysik, Karl-Schwarzschild-Str. 1, Postfach 1317, D-85741 Garching, Germany*
[3] *University of Turku, Turku, Finland*

Received November 7, 2017

Abstract—We analyze a long (with a total exposure time of 120 ks) X-ray observation of the unique Galactic microquasar SS 433 carried out by the XMM-Newton space observatory with the goal of searching for the fluorescent line of neutral (or weakly ionized) nickel at energy 7.5 keV. We consider two models for the formation of fluorescent lines in the spectrum of SS 433: (1) through the reflection of radiation from a putative central X-ray source off the optically thick neutral gas of the supercritical disk "funnel" walls; and (2) due to the scattering of the radiation coming from the hottest parts of the jets in the optically thin wind of the system. We show that for these two cases the flux of the Ni I K_α fluorescent line is expected to be 0.45 of the flux of the Fe I K_α fluorescent line at 6.4 keV for the relative nickel overabundance $Z_{\rm Ni}/Z = 10$ observed in the jets of SS 433. For the continuum model without the absorption edge of neutral iron, we have found an upper limit on the flux of the narrow Ni I K_α fluorescent line of 0.9×10^{-5} phot s^{-1} cm^{-2} (90% confidence level). In the continuum model with the absorption edge we have determined an upper limit on the flux of the Ni I K_α line at the level of 2.5×10^{-5} phot s^{-1} cm^{-2}. At the same time, the flux of the fluorescent iron line has been measured to be $9.9^{11.2}_{8.4} \times 10^{-5}$ phot s^{-1} cm^{-2}. This result implies that the nickel overabundance in the accretion disk wind should be at least a factor of 1.5 times smal than the corresponding nickel overabundance observed in the jets of SS 433.

DOI: 10.1134/S1063773718060038

Keywords: *black holes, neutron stars, accretion, jets, SS 433.*

1. INTRODUCTION

SS 433 is currently the only known Galactic X-ray binary system in which a continuous, highly supercritical regime of accretion is realized with a specific accretion rate $\dot{m} = \dot{M}/\dot{M}_{\rm Edd} \sim 400$, $\dot{M}_{\rm Edd} = 3 \times 10^{-8} \left(\frac{M}{M_\odot}\right) M_\odot$ yr^{-1}, where M is the mass of the compact object (for a review, see, e.g., Fabrika 2004). For this regime the standard theory of disk accretion predicts the presence of intense mass outflows both in the form of an accretion disk wind and in the form of relativistic jets (Shakura and Sunyaev 1973). The wind is predicted to be launched from a distance of the order of the accretion flow spherization radius, $R_{\rm sp} \sim \dot{m} R_{\rm in}$, for an inner accretion disk radius $R_{\rm in} = \frac{6GM}{c^2} \sim 10^6 \left(\frac{M}{M_\odot}\right)$ cm, where G is the gravitational constant and c is the speed of light. At the same time, the jets are apparently launched from regions in the immediate vicinity of the compact object, i.e., at a distance of $\sim 10 R_{\rm in}$. Despite the fact that this general picture, on the whole, is confirmed by recent numerical simulations (Ohsuga and Mineshige 2011; Fender and Gallo 2014), the specific mechanisms that determine the actual properties of such outflows, in particular, their geometry, velocity, and transferred mass and energy flows, still remain unclear. On the other hand, it seems very important to develop the methods of measuring the outflow parameters from observations and the methods of comparing theoretical models with observations.

The properties of relativistic jets have been studied relatively well owing to their intense X-ray radiation. The latter is well described by the model of a nearly ballistic, moderately relativistic mass flow that becomes visible to a distant observer at the instant its temperature is $T_0 \sim 30$ keV.[1] As the matter recedes

*E-mail: tomedvedev@iki.rssi.ru

[1] In what follows, the temperature is expressed in energy units kT, where k is the Boltzmann constant.

from the base, it cools down through adiabatic expansion and radiative energy losses until the temperature reaches $T \sim 0.1$ keV (Brinkmann et al. 1996; Kotani et al. 1996; Marshall et al. 2002; Khabibullin et al. 2016). Thereafter, thermal instability apparently develops in the gas and fragmentation of the jets occurs (Brinkmann et al. 1988). As a result, the X-ray spectrum of the jets is a combination of the thermal bremsstrahlung continuum coming from the hottest regions and the set of emission lines corresponding to transitions in highly ionized (hydrogen- and helium-like) atoms of heavy elements, in particular, silicon, sulfur, iron, and nickel, which are produced predominantly in regions with temperatures that ensure the maximum plasma emissivity in a given line.

Like the situation with the observed optical emission lines, the positions of the X-ray lines turn out to be shifted due to a combination of the longitudinal and transverse Doppler effects. The Doppler shift of each of the jets changes periodically with time, which is explained by a change in the direction of the jets relative to the line of sight as a consequence of their precession (Abell and Margo 1979; Fabian and Rees 1979; Milgrom 1979).

An important fact is that the relative intensities of the emission lines and their ratios to the continuum intensity point to a nearly solar chemical composition of the jet plasma (see, e.g., Kotani et al. 1996; Marshall et al. 2002). However, the nickel abundance measured in this way turns out to be larger than the solar one by a factor of ~10 (Kotani et al. 1996; Brinkmann et al. 2005; Medvedev and Fabrika 2010). In this case, in view of the significant transverse velocity gradient caused by ballistic gas expansion, the observed nickel overabundance cannot be explained, for example, by more efficient resonant scattering (and, as a consequence, by a redistribution of some of the photons into the broad line wings due to their scattering by hot electrons; see Sazonov and Sunyaev 2000) in the lines of other, more abundant and, consequently, optically thicker (for resonant scattering) elements, primarily iron, sulfur, and silicon (Khabibullin and Sazonov 2012)). The causes of the emergence of a nickel overabundance in the jet matter remain unclear and may be associated both with the physical conditions and jet launching mechanisms, its subsequent propagation until it becomes directly visible to an observer, and with the chemical peculiarities of the companion star.

From this point of view, it seems important to try to also measure the nickel abundance in the matter of the accretion disk wind, the mass flow in which ($\sim\dot{M}$) in reality can exceed the mass flow in the jets ($\sim\dot{M}_{\rm Edd}$; see, e.g., Khabibullin et al. 2016) by several orders of magnitude. The accretion disk wind "sees" the radiation from the hotter jet regions hidden from the observer, through which it manifests itself in X-rays by blocking, reprocessing, and partially scattering this radiation and, possibly, the radiation from the putative central source. The latter scenario was proposed by Medvedev and Fabrika (2010) to explain the excess of continuum radiation in the spectrum of SS 433 above 3 keV relative to the predictions of the jet emission model and the observed fluorescent Fe I K_α line of neutral (or weakly ionized) iron with a flux of 10^{-4} phot s^{-1} cm^{-2} (Kotani et al. 1996; Marshall et al. 2002; Brinkmann et al. 2005; Kubota et al. 2010; Medvedev and Fabrika 2010; Khabibullin et al. 2016).

The position (6.4 keV) and width ($\Delta v_{FWHM} <$ 1000 km s^{-1}) of the fluorescent iron line lead to the conclusion that the medium in which it is formed is fairly cold and without significant line-of-sight velocity dispersion. However, the separation of the component directly associated with the scattered radiation from the total observed continuum is also required to reconstruct a more complete picture of the geometry and physical properties (for example, the abundances of heavy elements) of this medium. In principle, such a separation is possible by determining the contribution of the jet emission over the soft X-ray spectral region (below 3 keV). In this region the contribution of the additional hard X-ray component is small and quite a few spectral lines are present, while modern X-ray spectrometers (for example, Chandra/HETGS) are characterized by the greatest sensitivity and resolution (Khabibullin et al. 2016). Another principal possibility is to investigate the variability of the observed radiation and its spectral dependence, in particular, the cross-correlation properties of the radiation in different energy ranges.

An additional possibility of investigating the medium responsible for the fluorescent radiation is related to the search for fluorescent lines from other elements; the ratio of their intensity to the intensity of the fluorescent iron line would allow the abundance ratio of different elements to be judged. For example, in the case of nearly solar heavy element abundances, the fluorescent Ni I K_α line at 7.5 keV is expected to be a factor of 20 weaker than the fluorescent Fe I K_α line at 6.4 keV, so that its detection seems to be a fairly difficult task even for sources with a sufficiently bright iron line. Nevertheless, the fluorescent nickel line is still detected in the X-ray spectra of obscured active galactic nuclei (Molendi et al. 2003; Fukazawa et al. 2016). In the case of a tenfold nickel overabundance, as is observed in the jets of SS 433, the expected flux of the Ni I K_α line turns out to be only approximately half the flux of the Fe I K_α line, i.e., at a level of 6×10^{-5} phot s^{-1} cm^{-2}. In principle, this is enough for reliable detection in the available archival data, which contain a total of

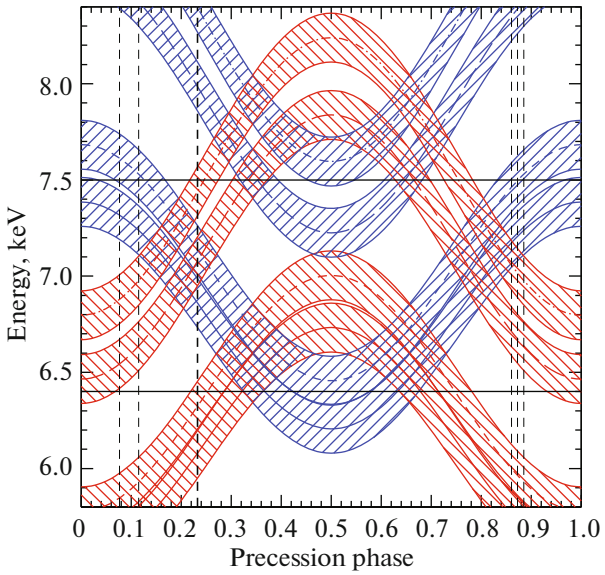

Fig. 1. (Color online) Predicted positions of the brightest X-ray lines of the approaching (blue lines) and receding (red lines) jets as a function of the precession phase of SS 433. The Fe XXV K_α ($E_0 = 6.7$ keV, solid lines), Fe XXVI Ly_α ($E_0 = 6.96$ keV, short dashes), Ni XXVII K_α ($E_0 = 7.8$ keV, long dashes), and Ni XXVIII Ly_α ($E_0 = 8.1$ keV, dash–dotted line) lines are shown. The hatched areas depict the "region of influence" for each line. This region is defined so that the intensity of the line convolved with the EPIC-pn/XMM-Newton response matrix drops by a factor of 10 with respect to the peak value at the region boundary (i.e., the half-width $\delta E = \sqrt{2\ln(10)}\Sigma_E$ and $\Sigma_E \approx 60$ eV correspond to $\Delta E_{FWHM} = 140$ eV). It is assumed that the positions of the fluorescent Fe I K_α (6.4 keV) and Ni I K_α (7.5 keV) lines do not change with precession phase; they are indicated by the horizontal black lines. The precession phases of the available XMM-Newton out-of-eclipse observations are indicated by the vertical dashed lines; the thick line corresponds to the observation used here.

several hundred kiloseconds of SS 433 observations with X-ray spectrometers.

Unfortunately, this approach involves considerable difficulties in practice. On the one hand, the sensitivity of the Chandra high-resolution grating spectrometers drops sharply at energies above 7 keV, which makes the search for such weak features near 7.5 keV difficult, given the the spectral variability of the source caused by the "motion" of the jet lines, and also because of the absence of a completely self-consistent continuum model in the spectral region under consideration (for example, the presence of a neutral iron absorption edge is possible at energies above 7.1 keV). On the other hand, the XMM-Newton EPIC-pn spectrometer has a significant effective area up to an energy of ~10 keV, which in principle makes it possible to detect the line of interest with a high significance. Nevertheless, the spectral resolution of this instrument is relatively low, $\Delta E_{FWHM} = 140$ eV at 7 keV, which potentially leads to contamination of the spectral range of interest by the emission of much brighter and instrumentally broadened lines from the relativistic jets.

In this paper we reviewed the available XMM-Newton archival data and chose the observation best suited to the search for the Ni I K_α line, given the achievable sensitivity, the source's brightness, and its precession phase. A combination of the high EPIC-pn sensitivity and the nearly optimal time of observation has allowed us to constrain the nickel overabundance in the supercritical accretion disk wind using X-ray fluorescence for the first time.

The paper is organized as follows. The data are described in Section 2. The possibility of obtaining the constraints on the flux of the fluorescent Ni I K_α line from them by taking into account the precessional motion of the considerably brighter jet emission lines is briefly discussed. The spectral emission models that are used to analyze the data in the spectral range of interest are described in Section 3. In Section 4 the described models of the continuum and line emission components are used to analyze the spectral data. We determine the constraints on the flux in the Ni I K_α line, depending on the assumptions about the spectral shape in the immediate vicinity of the line. In Section 5 the derived constraints on the flux of the Ni I K_α line are discussed in terms of its ratio to the flux of the Fe I K_α line. We infer the relative nickel abundance in the wind of SS 433. Section 6 contains our conclusions. A detailed description of the method of determining the errors in the derived parameters and the fluxes of the investigated fluorescent lines, which are extremely important for understanding the compatibility of the chemical composition of the system's jets and wind, is given in the Appendix.

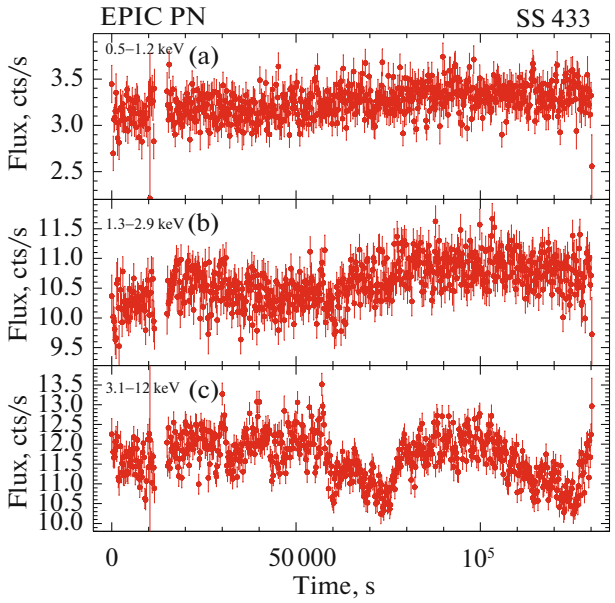

Fig. 2. (Color online) EPIC-pn/XMM-Newton light curves of SS 433 on October 3–5, 2012, in the 0.5–1.2 (a), 1.3–2.9 (b), and 3.1–12 keV (c) energy bands.

2. OBSERVATIONAL DATA

We analyzed all out-of-eclipse observations of SS 433 in the XMM-Newton data archive to select the observations best suited to searching for the fluorescent Ni I K_α line at 7.5 keV from the viewpoint of "contamination" of the region under consideration by the much brighter emission lines of the jets. The results of this analysis are shown in Fig. 1, where the vertical dashed lines indicate all out-of-eclipse data. The 2012 observation (*ObsID* 694870201, principal investigator A. Medvedev), which served as a basis for the presented work (indicated by the thick dashed line), corresponds to the precessional and orbital phases of SS 433 $\psi = 0.24$ and $\phi = 0.44$–0.55, respectively (according to the ephemeris from Goranskij (2011)). The spectral lines of the approaching jet marked by the blue curves in Fig. 1 are the brightest lines in the X-ray spectrum of SS 433 and, as a rule, are brighter than the corresponding lines of the receding jet (marked by the red curves) by a factor of 3–4 due to the relativistic boosting and possible absorption effects (for more details, see Kotani et al. 1996; Marshall et al. 2002). For this reason, the observation under consideration is the most optimal one among all the available XMM-Newton archival data.

The XMM-Newton observation *ObsID* 694870201 was performed on October 3–5, 2012. The primary data reduction was carried out using the standard Science Analysis Software (SAS) of version 13.0. In the first step, we selected all of the events that were not affected by proton flares. The net effective exposure for the EPIC-pn instrument was ≈124 ks.

Owing to the high brightness of SS 433 corresponding to an average count rate from the source of about 25 counts/s, the EPIC-pn camera operated in the timing mode that allowed bright objects to be observed. The final data reduction was carried out in accordance with the standard user guide.[2] In particular, we extracted the background photons from pixel rows 2–16 and the photons belonging to the source from rows 29–47. As a result, we obtained the light curves (see Fig. 2) and spectra averaged both over the entire exposure and over 10 ks, which allows us to investigate the spectral evolution of the source with good statistics. In this paper we use unbinned spectra. We also checked that an analysis of the spectra binned by 25 counts per energy channel gives consistent results within the error limits (see also the Appendix).

3. SPECTRAL MODELS

3.1. Baryonic Jets

The spectral model of the thermal X-ray emission from baryonic jets in the range of parameters expected for SS 433 was computed and made publicly accessible by Khabibullin et al. (2016) (hereafter the `bjet` model). The model is based on the solution of the thermal balance equation with a self-consistent allowance for the radiative energy losses by the gas.

[2] `www.cosmos.esa.int/web/xmm-newton/sas-threads/.`

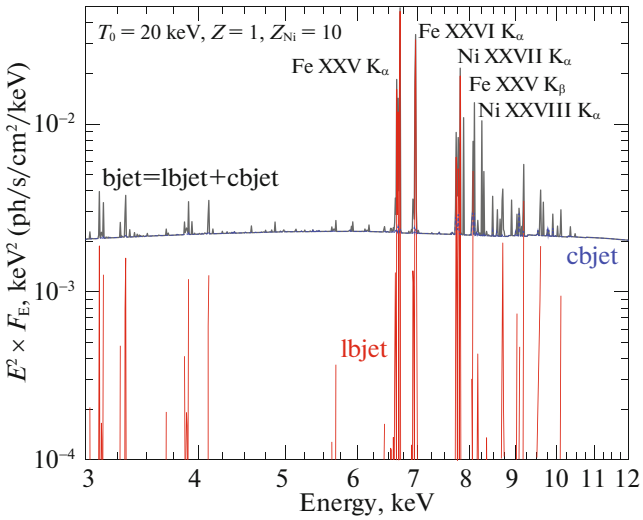

Fig. 3. (Color online) Spectral models of the thermal X-ray emission from the baryonic jets in SS 433. The black line indicates the spectral energy distribution obtained in the `bjet` model for the jet parameters $L_k \times \tau_{e0} = 0.5 \times 10^{38}$ erg s^{-1}, $T_0 = 20$ keV, $Z = 1$, and $Z_{Ni} = 10$. The blue dotted line indicates the continuum component (in sum with the pseudo-continuum)—the `cbjet` model. The red line indicates the `lbjet` line emission model determined by the difference `bjet`−`cbjet`. The predicted flux is reduced to distance $D = 10$ kpc to the emission source. The lines that are considered in terms of a phenomenological model in Section 4 are also labeled in the figure.

This allows the emission measure distribution in the range of temperatures corresponding to both continuum emission (mostly the hottest parts of the jet) and line emission (parts of the jet with $T < 10$ keV) to be reproduced with a high accuracy. The overall spectrum of the model is determined by adding the contributions from thin single-temperature transverse layers along the jet whose emission is calculated in the regime of a hot, optically thin plasma in collisional ionization equilibrium (CIE) based on the `AtomDB/APEC` database[3] (version 3.0.9, Foster et al. 2012). The input parameters of the bjet model adapted to analyze the data for SS 433 (fixed gas bulk velocity $\beta = v/c = 0.26$ and half-opening angle $\Theta = 0.02$) include the kinetic luminosity L_k, the gas temperature at the jet base T_0 (the jet region closest to the compact object that is directly visible to an observer is called the jet base), the optical depth for electron scattering at the jet base τ_{e0}, the abundance of heavy elements Z (except for nickel), and a separate parameter for the nickel abundance $Z_{\rm Ni}$. The abundance parameters are specified relative to the solar chemical composition (Anders and Grevesse 1989). The shape of the spectrum obtained in the model is determined by the distribution of the differential emission measure along the jet and depends only on α, which is a combination of model parameters:

$$\alpha = \frac{2}{3}\frac{\tau_{e0}}{\Theta\beta}\frac{\Lambda_Z(T_0)}{\sigma_e c T_0}\frac{X}{1+X}, \qquad (1)$$

where $\Lambda_Z(T_0)$is the plasma emissivity, $X = n_i/n_e \approx 0.91$ is the ion-to-electron ratio, and $\sigma_e = 6.65 \times 10^{-25}$ cm^2 is the Thomson cross section. If the radiative losses are assumed to be due to only the hydrogen and helium bremsstrahlung, then we can obtain a simple estimate: $\alpha \approx 4.42\,\tau_{e0} \times \left(\frac{10\,\text{keV}}{T_0}\right)^{1/2}$. The gas cooling is determined by the adiabatic expansion of the jet for $\alpha \ll 1$ and by the radiative energy losses for $\alpha \gg 1$ (for more details, see Khabibullin et al. 2016).

The `AtomDB` database also allows the continuum emission[4] and the line emission determined by the plasma emissivity at a given temperature to be analyzed separately. In this paper we use this possibility to extract the separate continuum component from the total (over the temperature distribution along the jet). As a result, we computed a new version of the `bjet` model for a similar grid of parameters and energies, but containing only the continuum component (hereafter the `cbjet` model[5]). Thereafter, by subtracting the `cbjet` model from the total jet emission, we can determine the lines-only emission model (hereafter the `lbjet=bjet-cbjet` model). In this paper we use the `lbjet` model as the main tool for analyzing the emission lines in the X-ray jets of

[3] `http://www.atomdb.org`

[4] In addition to the thermal bremsstrahlung continuum, the so-called pseudo-continuum of the `APEC` model includes two-photon and recombination continua as well as very weak lines.

[5] The model is publicly accessible and can be downloaded from the web site: `http://hea133.iki.rssi.ru/public/bjet/.`

SS 433 in the spectral region of interest. Examples of the spectra for the same set of parameters of the `bjet`, `cbjet`, and `lbjet` models are shown in Fig. 3.

In Section 4, in addition to analyzing the data using the `lbjet` model, we also use a phenomenological approach (hereafter the phenomenological model) to describe the main spectral features in the energy range 6–9 keV in the form of individual Gaussians. Khabibullin et al. (2016) computed the model predictions for a similar set of spectral parameters (the ratio of the fluxes in bright lines, the photon index, etc.) that allow such parameters of the jets as the gas temperature near their base and the abundance of heavy elements to be estimated even when analyzing low-spectral-resolution data. The agreement between the two approaches in the predictions of jet parameters should serve as an additional criterion for the adequacy of the models used.

3.2. Optically Thick Reflection

Medvedev and Fabrika (2010) proposed a model in which the additional hard component and the fluorescent Fe I K_α line emerge when the radiation from the putative central X-ray source is reflected off the walls of the supercritical disk funnel. The luminosity of the central source required in this model turns out to be great, $\sim 10^{40}$ erg s^{-1}. This, however, may actually be true, bearing in mind that a highly supercritical regime of accretion is realized in the system and that the system is observed nearly edge-on and the emission collimated along the axis of the supercritical accretion disk can easily avoid direct detection. In this model SS 433 would manifest itself as an ultraluminous X-ray source if the observer could see it along the disk axis (Begelman et al. 2006; Poutanen et al. 2007; however, see Khabibullin and Sazonov (2016) for an upper luminosity limit).

As an approximation of the reflected spectrum arising in such a scenario, we use the `pexmon` model (Nandra et al. 2007; see also the paper by George and Fabian (1991) on which it is based) available in the XSPEC software (Arnaud 1996). It allows one to self-consistently predict the intensities of fluorescent iron and nickel lines and the absorption edges corresponding to these elements in the case of reflection of the radiation from a source isotropically illuminating a semi-infinite slab of neutral gas with a specified abundance of heavy elements. The spectrum of the incident radiation is a power law with a photon index Γ and an exponential cutoff at high energies proportional to e^{-E/E_c}. At fixed Γ and E_c the shape of the reflected spectrum is determined by the angle i between the line of sight and the normal to the reflecting slab. In the model proposed by Medvedev and Fabrika (2010) the inclination of the line of sight to the walls of the supercritical disk funnel is expected to be nearly perpendicular. Figure 4 shows how the shape of the reflected spectrum changes as the angle i varies in the range from 10° to 60°. The spectrum of the source is assumed to be a power law with a slope $\Gamma = 1.5$, which roughly corresponds to the spectrum of the hot parts of the SS 433 jets. Apart from the Fe I K_α line, the fluorescent Fe I K_β line at 7.06 keV emitted during the electron transition from the M-shell is clearly seen in Fig. 4. The flux of the Fe I K_β line is ≈11% of the flux of the Fe I K_α line (see, e.g., Kaastra and Mewe 1993).

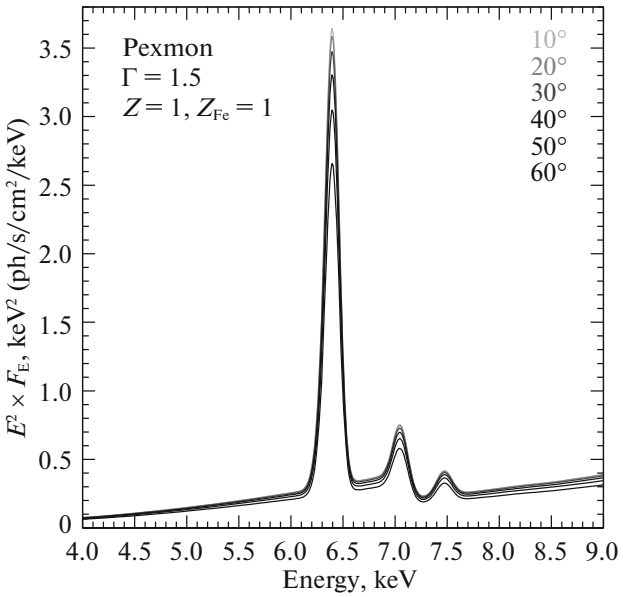

Fig. 4. Predicted shape of the reflected spectrum in the `pexmon` model (without the direct contribution from the illuminating source) as a function of the angle i between the line of sight and the normal to the semi-infinite slab of neutral matter, illuminated by isotropic X-ray source. The spectrum of the illuminating source is a power law with a photon index $\Gamma = 1.5$. The abundance of heavy elements in the reflecting matter is specified to be solar one.

An analysis of the spectra predicted by the model shows that the Ni I K_α-to-Fe I K_α flux ratio does not depend on the direction of observation (angle i). The fluorescent yield of K-shells increases with charge number of the atomic nucleus (see, e.g., Bambynek et al. (1972) for a review). For the solar abundance of heavy elements (Anders and Grevesse 1989) the ratio of the photon fluxes in the fluorescent nickel and iron lines can be estimated as

$$R_{\rm fluor}(Z_{\rm Ni}=1) = \frac{F(\text{Ni I K}_\alpha)}{F(\text{Fe I K}_\alpha)} \sim \frac{n_{\rm Ni\,I}}{n_{\rm Fe\,I}} \frac{\omega_{\rm Ni\,I\,K\alpha}}{\omega_{\rm Fe\,I\,K\alpha}} \approx 0.045, \quad (2)$$

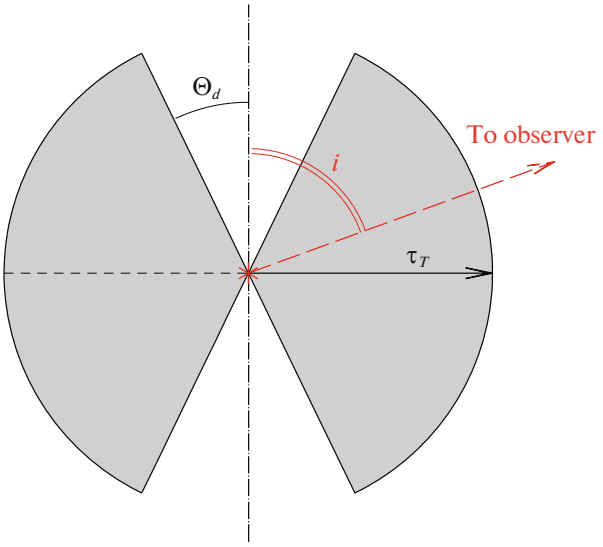

Fig. 5. (Color online) Geometry of the `cwind` model for optically thin scattering. The illuminating source is assumed to be placed at the center of a homogeneous spherical cloud of neutral gas with a radial Thomson optical depth τ_T in which symmetric conical cavities with a half-opening angle $\Theta_d = \arccos\mu_d$ were cut out along the axis passing through the cloud center and making an angle $i = \arccos\mu$ with respect to the observer's line of sight.

where $\omega_{\rm Ni\,I\,K\alpha} = 0.41$ and $\omega_{\rm Fe\,I\,K\alpha} = 0.34$ are the fluorescent yields for Ni I K_α and Fe I K_α, respectively (Bambynek et al. 1972). Such a simple estimate agrees well with the predictions of the `pexmon` model for $R_{\rm fluor}$ assuming the solar abundance of elements. As long as the probability of the photoabsorption of an incident photon by nickel atoms is smaller than the total probability of its absorption by atoms of other elements or its scattering by electrons, the flux in the Ni I K_α line and, hence, the ratio $R_{\rm fluor}$, increases linearly with increasing nickel abundance in the reflecting medium. In the region of interest, $Z_{\rm Ni} \sim 10$, this is actually the case, because the opacity of the medium for photoabsorption begins to be dominated by absorption by nickel atoms only for $Z_{\rm Ni} > 20$. Therefore, in the case of a tenfold nickel overabundance in the wind of the supercritical SS 433 disk, the flux ratio is expected to be $R_{\rm fluor}(Z_{\rm Ni} = 10) \approx 0.45$. The `pexmon` model does not allow this prediction to be tested, but we tested this assertion using the `cwind` scattering model in the next subsection (see Fig. 7). Note also that our conclusions based on the `pexmon` model are consistent with the results of observations and modeling of the reflected radiation in the spectra of obscured AGNs (Yaqoob and Murphy 2011; Molendi et al. 2003).

3.3. Optically Thin Scattering

In this paper we for the first time propose an alternative explanation for the emergence of the hard component and the fluorescent iron line in the X-ray spectrum of SS 433, i.e., that the hard component is the radiation from the hottest jet parts absorbed almost completely in the soft X-ray band and only slightly modified in the hard X-ray band due to its passage through the region of the supercritical accretion disk wind that is optically thin for Thomson scattering ($\tau_T \sim 0.1$), but optically thick for photoabsorption at energies below 3 keV. Since in this model the hard X-ray radiation is attenuated only slightly, there is no need for a bright central source, only a small fraction of whose radiation would be intercepted by the reflector. The fluorescent Fe I K_α line emerges in such a situation together with the scattered continuum, whose contribution to the total observed spectrum, however, turns out to be τ_T, i.e., it is relatively small.

We performed Monte Carlo simulations using the `cwind` spectral model. A detailed description of the code is given in Churazov et al. (2017), where a similar model for the illumination of a spherical molecular cloud by an external source (`crefl` model[6]) is presented. A similar analysis for AGNs is presented in Sazonov et al. (2015). The code includes a complete calculation of the radiative transfer with Compton scattering, photoabsorption, and fluorescence by neutral atoms of the most abundant heavy elements. In the `cwind` model the radiation source is assumed to be placed at the center of a homogeneous spherical cloud of neutral gas with a radial Thomson scattering depth τ_T and a heavy-element abundance Z in which two symmetric conical cavities with a half-opening angle $\Theta_d = \arccos\mu_d$ were cut out along the axis passing through the cloud center and making an angle $i = \arccos\mu$ with the observer's line of sight (see Fig. 5). The source's spectrum is specified by the model of thermal bremsstrahlung with a gas temperature T_b. Furthermore, the nickel overabundance with respect to the solar composition $Z_{\rm Ni}$ was included as an additional model parameter.

Despite the obvious simplicity of the model, it encompasses a great variety of spectral shapes that result from combining the scattered and directly transmitted radiations for various parameters τ_T, μ, μ_d, and $Z_{\rm Ni}$ (see Fig. 5). For a reasonable range of gas temperatures at the jet base ($T_b \sim 20$–30 keV) the spectral shape of the radiation changes only slightly with varying parameter T_b.

In Fig. 7 the red dashed ($T_b = 25$ keV) and dash–dotted ($T_b = 35$ keV) lines indicate the ratios of the photon fluxes of the fluorescent lines $R_{\rm fluor} =$

[6] `http://www.mpa-garching.mpg.de/~churazov/crefl/`

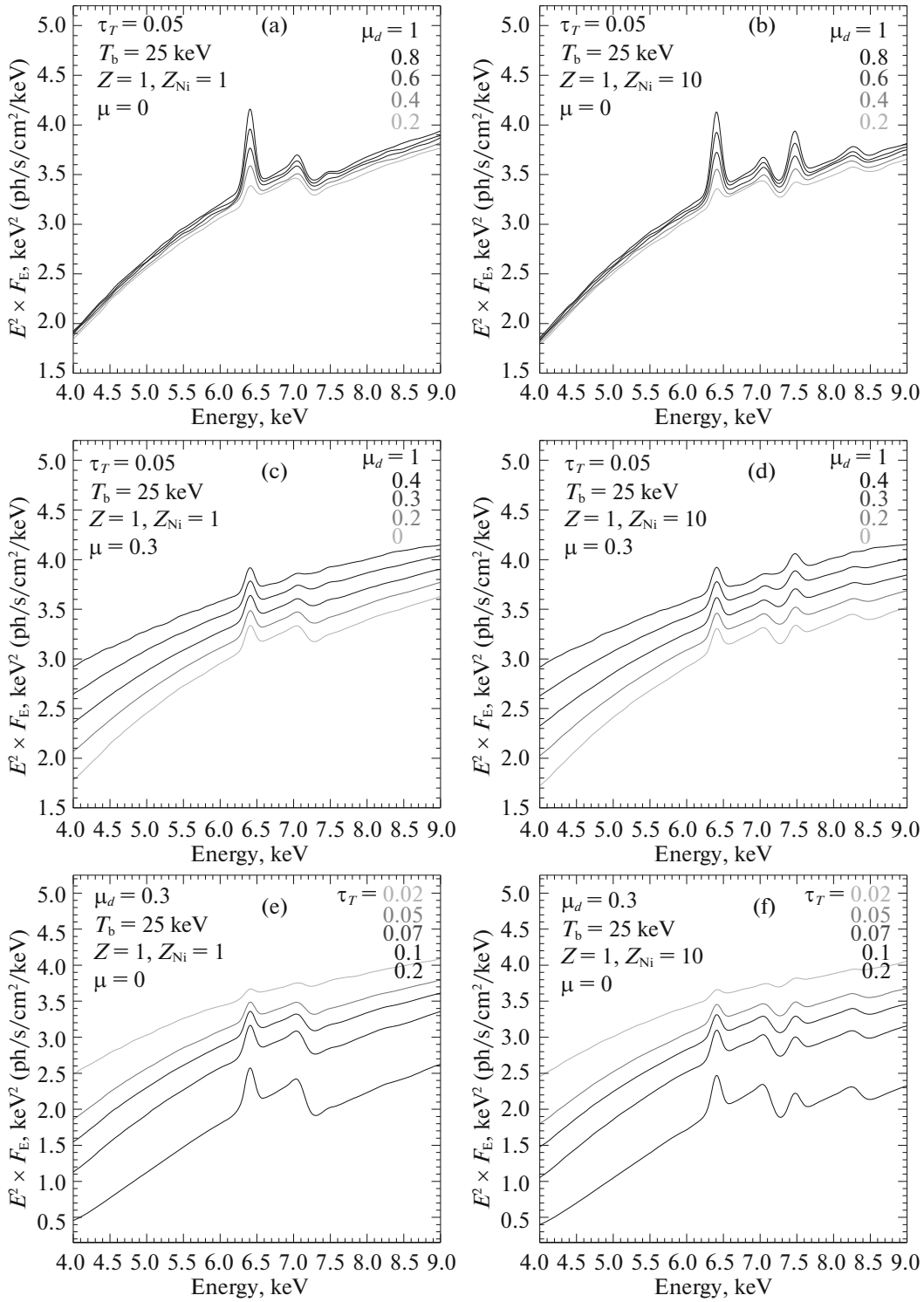

Fig. 6. Spectra of the jet emission that passed through an optically thin cloud of cold gas calculated using the `cwind` model for various sets of model parameters. The left and right panels show the results for the solar chemical composition of the scattering gas and for the relative nickel overabundance $Z_{\rm Ni}/Z = 10$, respectively. The two upper panels show the spectrum of the scattered component for various half-opening angles of the supercritical disk wind funnel μ_d (see Fig. 5). The two middle panels show the dependence on the angle between the observer's line of sight and the disk axis $\mu = \cos i$. The lower panels show the dependence on the Thomson optical depth along the cloud equator τ_T.

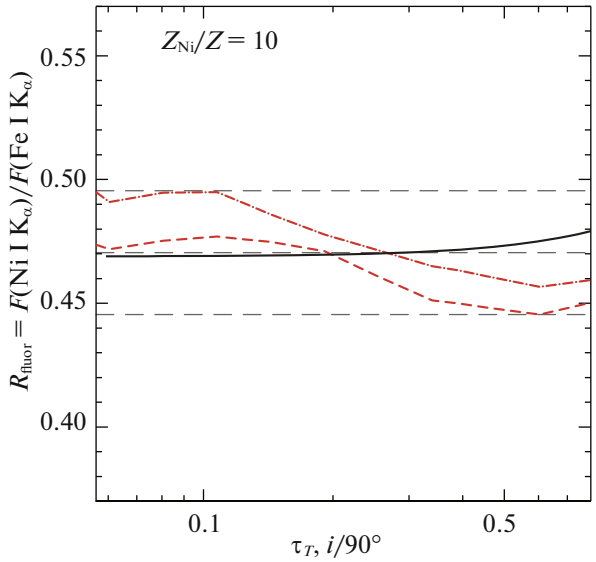

Fig. 7. (Color online) Predicted ratios of the photon fluxes of the fluorescent Ni I K_α 7.5 keV and Fe I K_α 6.4 keV lines for two models of their formation: (a) when the radiation is reflected from an optically thick slab (`pexmon` model, solid line), in this case, the inclination i of the line of sight with respect to the normal to the slab is shown along the horizontal axis; (b) when the radiation passes through an optically thin gas cloud calculated in the `cwind` model for bremsstrahlung temperatures $T_0 = 25$ (red dashed line) and $T_0 = 35$ keV (red dash–dotted line). In this case, the Thomson optical depth of the cloud τ_T is shown along the horizontal axis. The flux ratio is displayed for the nickel abundance in the reflecting/scattering matter $Z_{Ni} = 10$ relative to the solar chemical composition. The black dashed horizontal lines indicate the minimum, average, and maximum values of the flux ratio R_{fluor}.

$F(\mathrm{Ni\ I\ K}_\alpha)/F(\mathrm{Fe\ I\ K}_\alpha)$ calculated for the `cwind` model as a function of the cloud optical depth τ_T and with the relative nickel abundance $Z_{Ni}/Z = 10$. The black solid line in the same figure indicates the value of R_{fluor} found from the `pexmon` model and *multiplied by 10* as a function of the inclination i of the line of sight to the reflecting slab. As can be seen from the figure, the flux ratio lies in the range 0.45–0.5 and depends weakly on the model parameters. The linear dependence of R_{fluor} on the relative nickel abundance is well confirmed by the agreement between the results of the two models.

4. RESULTS

4.1. The Continuum Model

In the first step of our work with the data, it is necessary to determine the shape and level of the continuum in the energy range 6–9 keV, where, apart from the fluorescent lines of interest, the brightest emission lines of the jets are emitted. Unfortunately, this cannot be done completely self-consistently, because there is still no clear understanding of the processes responsible for the continuum formation in this spectral region. As was shown by Khabibullin et al. (2016), the `bjet` spectral model can describe well the soft part (<3 keV) of the SS 433 spectrum even in the case of data with a high spectral resolution. However, a noticeable excess of hard X-ray radiation is observed at higher energies. In particular, this manifests itself in the slope of the spectrum in the range 3–6 keV (photon index $\Gamma \lesssim 1.5$) containing no bright spectral lines that cannot be reproduced by the multi-temperature thermal jet radiation model alone (see Fig. 7 in Khabibullin et al. 2016; Brinkmann et al. 2005; Medvedev and Fabrika 2010). It is quite probable that the component of the radiation from the hottest parts of the jets scattered by the optically thin wind but, at the same time, suppressed in the soft X-ray band due to photoabsorption contributes to the hard part of the spectrum (see Section 3). In this sense the study of SS 433 based on a large volume of RXTE data (Filippova et al. 2006) is noteworthy. It showed that the shape of its spectrum at energies up to 50 keV, on the whole, agrees well with the bremsstrahlung spectrum of a plasma with a temperature ~20–30 keV. Interestingly, the speed of sound in the gas corresponding to such a temperature is comparable to the transverse expansion velocity of the jets at an opening angle of ~1.5° (Marshall et al. 2002). Nevertheless, other scenarios for the formation of the hard component are also possible, such as the reflection of radiation from the hidden powerful central source by the opaque walls of the supercritical disk funnel (Medvedev and Fabrika 2010) or the Comptonization of soft X-ray photons by hot electrons in the hypothetical disk corona (Cherepashchuk et al. 2009; Krivosheyev et al. 2009).

We are interested in searching for spectral features near the Ni I K_α line at 7.5 keV. Therefore, as a continuum model we use the single-temperature bremsstrahlung spectrum whose parameters are determined in the spectral regions containing no bright emission lines: 4.3–5.8 and 10–12 keV.[7] The derived continuum parameters, the temperature $T = 22.3^{23.2}_{21.5}$ keV and the 6–9 keV flux $F_{6-9} = 4.22^{4.24}_{4.20} \times 10^{-11}$ erg s^{-1} cm^{-2}, are fixed in the subsequent analysis of the spectral lines. Here and below, the range of parameters is specified for a 90% confidence

[7] For the range 4.3–5.8 keV the lower boundary is determined so as to exclude the Ca XX Ly_α 4.1 keV doublet of the approaching jet, while the upper boundary excludes the Fe XXV K_α 6.7 keV triplet of the receding jet. The lower boundary of the range 10–12 keV excluded the Ni XXVIII Ly_β 9.6 keV line of the approaching jet, while the EPIC-pn effective area is almost zero at energies above 12 keV.

level (for more details on the method of estimating the errors, see the Appendix). The very low quality of the fit, corresponding to $\chi^2/\text{d.o.f} = 985/696 = 1.4$, is related to the source's spectral variability within the total exposure time (see Section 4.4).

4.2. The Phenomenological Method of Line Description

We will begin our analysis of the observed spectrum using simple spectral characteristics (see also Khabibullin et al. 2016) by describing the bright emission lines in the range 6–9 keV by individual Gaussians linked between themselves by the Doppler shifts corresponding to the radial velocities of the relativistic jets in the system. Such a method will be called a phenomenological model. The brightest observed X-ray lines in the energy range of interest correspond to the K_α and Ly_α transitions in helium-like and hydrogen-like iron and nickel ions, respectively. In addition, consider the line emitted during the K_β transition in helium-like iron, because it falls into the neighborhood of the Ni XXVII K_α and Ni XXVIII Ly_α lines important for our study. We will call the jet approaching the observer the "blue jet" (subscript b) and the oppositely directed jet the "red jet" (subscript r).

We will describe the fluorescent Fe I K_α line by a narrow Gaussian with a width $\Sigma_{\text{Fe I}} = 5$ eV[8] and a centroid $E_{\text{Fe I}} = 6.4$ keV (from an analysis of the HETGS/Chandra data, Marshall et al. 2002; Lopex et al. 2006). When fitting the data, we will consider the line centroid as a free model parameter whose lower and upper bounds are specified to be 6.4 and 6.5 keV, respectively.

It can be seen from Figs. 1 and 2 that the "motion" of the jet emission lines often leads to their mutual overlapping (blending) in the spectrum for a characteristic line width corresponding to the EPIC-pn spectral response function (see also E_{zb} and E_{zr} in Table 1). Within the phenomenological model under consideration this leads to degeneracy of the parameters of weak lines when they are blended with brighter lines in the spectrum. To constrain the flux in such lines, we introduce a number of simplifying assumptions.

(1) The flux of the Ni XXVII K_α line of the red jet is fixed to be equal to the flux of the corresponding line of the blue jet multiplied by the ratio of the fluxes of the Fe XXV K_α lines of the red and blue jets: $F_r(\text{Ni XXVII K}_\alpha) = F_b(\text{Ni XXVII K}_\alpha)\frac{F_r(\text{Fe XXV K}_\alpha)}{F_b(\text{Fe XXV K}_\alpha)}$.

(2) The flux of the Fe XXV K_β line of the red jet is specified in a similar way: $F_r(\text{Fe XXV K}_\beta) = F_b(\text{Fe XXV K}_\beta)\frac{F_r(\text{Fe XXV K}_\alpha)}{F_b(\text{Fe XXV K}_\alpha)}$.

(3) The Fe XXVI Ly_α line of the red jet is blended with the fluorescent Fe I K_α lines. In this case, it is difficult to constrain the line flux based on the flux of the corresponding line of the blue jet, because the emissivity of the hydrogen-like iron Ly_α doublet has a peak at higher plasma temperatures than those in the case of the helium-like iron K_α triplet. By experimenting with various fits, we came to the conclusion that it is appropriate to fix the fluxes of the overlapping lines to be equal to each other: $F_r(\text{Fe XXVI Ly}_\alpha) = F(\text{Fe I K}_\alpha)$. The Fe I K_α line flux obtained in this way agrees well with the results of our fitting by the `lbjet` model (see the next subsection) and the results of Chandra observations (Lopez et al. 2006).

(4) The Ni XXVIII Ly_α line of the red jet turns out to be near the Ni I K_α 7.5 keV line being investigated. In view of the above-described uncertainty in $F_r(\text{Fe XXVI Ly}_\alpha)/F_b(\text{Fe XXVI Ly}_\alpha)$, it is also difficult to constrain the flux $F_r(\text{Ni XXVIII Ly}_\alpha)$ based on the flux of the corresponding line of the blue jet. Since the goal of our study is the search for weak spectral features at 7.5 keV, this line is excluded from consideration when fitting the data.

Next, let us add a narrow Gaussian corresponding to the Ni I K_α line with a centroid $E_{\text{Ni I}} = 7.5$ keV and a width $\Sigma_{\text{Ni I}} = \Sigma_{\text{Fe I}} = 5$ eV. As with the Fe I K_α line, we will consider the line centroid as a free parameter in the range from 7.5 to 7.6 keV.

An analysis of the spectrum using our model shows that large residuals remain in the energy range 6.6–6.7 keV. Probably, they can be related to a spectral line (or a set of lines) disregarded in the model. For the derived parameters of the Doppler shifts no emission lines from the jets fall into this range. If different regions of the supercritical disk wind have different degrees of ionization, then the lines associated with iron fluorescence in the highly ionized part of the wind can fall into this range (see, e.g., Kallman et al. 2004). To get an acceptable quality of the fit, we will add a narrow Gaussian with a width $\Sigma < 5$ eV and a centroid at 6.6 keV to the described model. The best-fit parameters of such a line correspond to the centroid $E_0 = 6.63^{6.64}_{6.62}$ keV and a flux of $0.98^{1.04}_{0.92} \times 10^{-4}$ phot s^{-1} cm^{-2}. The line flux is well constrained from the data. The line centroid can correspond to the ionization state of iron XXII–XXIII. In what follows, we will not describe

[8] The dispersion parameter Σ_{E0} for the standard form of a Gaussian function will be called the width of a line with a Gaussian profile: $I(E) = F\frac{1}{(1+z)\Sigma_{E0}\sqrt{2\pi}}\exp\frac{-(E(1+z)-E_0)^2}{2\Sigma^2_{E0}}$, where z is the Doppler shift, F, E_0, and Σ_{E0} are the line flux, centroid, and dispersion in the rest frame of the emitter.

Table 1. The set of simulated lines within the phenomenological method of data description

Spectroscopic symbol	Blue jet			Red jet	
	E_0, keV	E_{zb}, keV	flux (eq. width), 10^{-4} phot s^{-1} cm^{-2} (eV)	E_{zr}, keV	flux (eq. width), 10^{-4} phot s^{-1} cm^{-2} (eV)
Fe XXV K_α	6.70	6.92	$7.17^{7.26}_{7.08}$ (379^{385}_{373})	6.13	$3.76^{3.83}_{3.70}$ (200^{203}_{196})
Fe XXV K_β	7.88	8.14	$0.6^{0.7}_{0.4}$ (40^{50}_{30})	7.20	$= F_b$(Fe XXV K_β)$\dfrac{F_r(\text{Fe XXV K}_\alpha)}{F_b(\text{Fe XXV K}_\alpha)}$
Fe XXVI Ly_α	6.97	7.20	$2.68^{2.76}_{2.61}$ (119^{123}_{116})	6.37	$= F$(Fe I K_α)
Ni XXVII K_α	7.80	8.05	$2.07^{2.13}_{2.02}$ (181^{185}_{174})	7.13	$= F_b$(Ni XXVII K_α)$\dfrac{F_r(\text{Fe XXV K}_\alpha)}{F_b(\text{Fe XXV K}_\alpha)}$
Ni XXVIII Ly_α	8.10	8.36	$0.87^{0.92}_{0.81}$ (71^{75}_{67})	7.41	$= 0$

Spectroscopic symbol	Fluorescent lines	
	E_0, keV	flux (eq. width), 10^{-4} phot s^{-1} cm^{-2} (eV)
Fe I K_α	$6.450^{6.456}_{6.441}$	$1.11^{1.15}_{1.07}$ (53^{55}_{51})
Ni I K_α	$7.500^{7.505}_{7.500}$	$0.26^{0.30}_{0.22}$ (16^{18}_{14})
Fe (XXII–XXIII K_α?)	$6.63^{6.64}_{6.62}$	$0.98^{1.04}_{0.92}$ (39^{41}_{36})

The positions of the unshifted line centroids E_0 correspond to the weighted mean energies of the corresponding triplets and doublets. The best-fit parameters are given for fitting the 120-ks spectrum in the energy range 4.3–12 keV by the sum of lines and a bremsstrahlung continuum with a temperature $T = 22.3^{23.2}_{21.5}$ keV and a flux $F_{6-9} = 4.22^{4.24}_{4.20} \times 10^{-11}$ erg s^{-1} cm^{-2}. The data were obtained with the XMM-Newton EPIC-pn camera. The ranges of parameters are specified for a 90% confidence level (for more details, see the Appendix). The positions of the shifted lines E_{zb} and E_{zr} were calculated from the best-fit parameters of the Doppler shifts: $z_b = -3.15^{-3.13}_{-3.18} \times 10^{-2}$ and $z_r = 9.38^{9.43}_{9.33} \times 10^{-2}$ for the blue and red jets, respectively. The line fluxes are given in the emitter's rest frame without allowance for the continuum flux. The fluxes of the Fe XXV K_β and Ni XXVII K_α lines of the red jet are determined via the fluxes of the corresponding lines of the blue jet. The flux of the Fe XXVI Ly_α line of the red jet is assumed to be equal to the flux of the Fe I K_α line. The Ni XXVIII Ly_α line of the red jet is not considered. The width of the jet lines is found to be $\Sigma_{E0,jet} = 76^{78}_{74}$ eV, the width of the fluorescent lines is fixed: $\Sigma_{\text{Ni I}} = \Sigma_{\text{Fe I}} = 5$ eV (for more details, see the text). The unidentified line with a width $\Sigma < 5$ eV that should be added to the model to avoid large residuals near 6.6 keV is denoted by Fe XXII–XXIII K_α (see Fig. 8). The quality of the fit corresponds to χ^2/d.o.f $= 2174/1526 = 1.42$ (the χ^2 value per degree of freedom).

this line, because the spectral resolution of the EPIC-pn detector is too low to investigate its profile and to draw any conclusions about its origin.

The observed spectrum is fitted by our model. The total number of free model parameters is 15: the jet line fluxes, the line width $\Sigma_{E0,\text{jet}}$ (assumed to be the same for all jet lines), the Doppler shifts z_b and z_r for the two sets of jet lines, the centroids and fluxes of the fluorescent lines, and the flux and position of the unidentified line. The results of our data fitting are presented in Table 1, the model with the best-fit parameters is shown in Fig. 8.

4.3. The Model of X-ray Emission from Baryonic Jets

Let us now turn from the phenomenological description of the bright emission lines to modeling the set of lines that should be formed in the system's jets. For this purpose, we will use the `lbjet` model (see Section 3). As has been noted above, a self-consistent analysis of the spectral lines and continuum is beyond the scope of this study. Therefore, we will fix the continuum shape and level, as before, in the spectral regions 4.3–5.8 and 10–12 keV containing no bright lines (see Section 4.1).

The `lbjet` model inherits the parameter space of the `bjet` model (for more details, see Section 3 and Khabibullin et al. 2016). However, in the context of describing the spectral lines, the gas temperature at the jet base T_0 and the relative nickel abundance Z_{Ni}/Z become the main model parameters. The abundance of the remaining chemical elements, as in the `bjet` model, is specified by the parameter Z in solar abundance units (Anders and Grevesse 1989). Assuming that the cooling of the jets in SS 433 near the base is attributable mainly to adiabatic expansion ($\alpha < 1$, Khabibullin et al. 2016), the kinetic luminosity L_k and the optical depth for electron scattering at the jet base τ_{e0} in this case will make sense only as

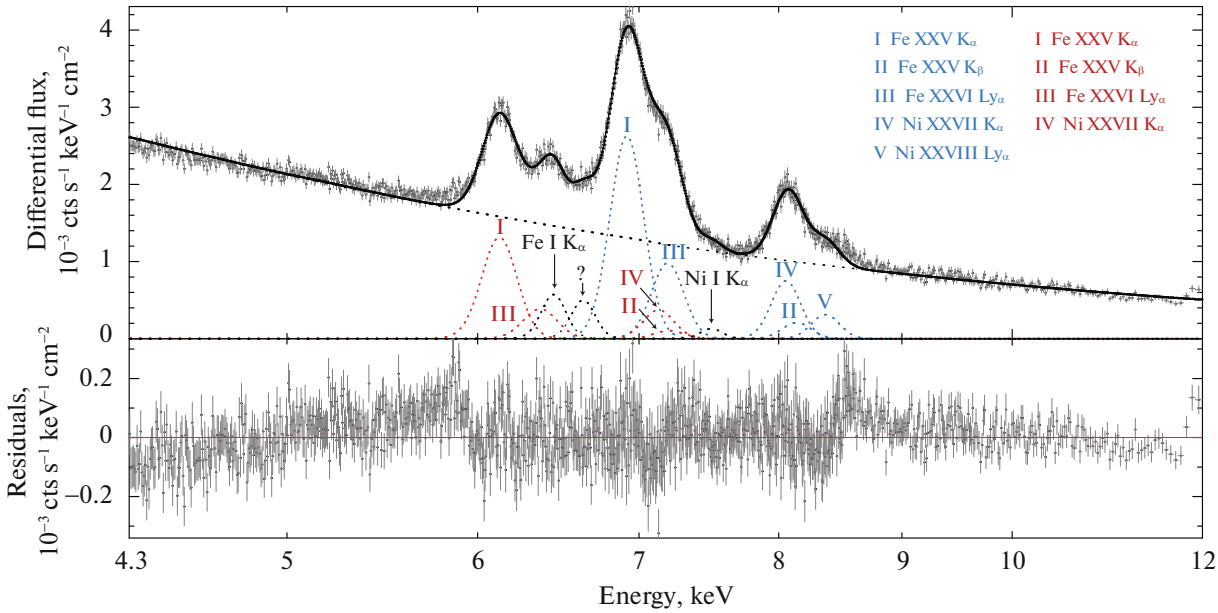

Fig. 8. (Color online) Phenomenological description of the jet emission lines and the fluorescent Fe I K_α 6.4 keV and Ni I K_α 7.5 keV lines in the SS 433 spectrum obtained with the XMM-Newton EPIC-pn camera with an exposure time of 120 ks. The blue and red symbols indicate the lines of the approaching and receding jets, respectively. The black symbols indicate the fluorescent lines and the unidentified line that should be added when fitting the observed spectrum (question mark).

the normalization quantities of spectral lines. For this reason, the parameter Z turns out to be degenerate and is not used during our fitting, we fix $Z = 1$. Moreover, we will assume the temperatures of the two jets to be equal to avoid the degeneracy between the flux in the Fe I K_α line (due to its blending with the Fe XXVI Ly_α line) and the temperature of the red jet. By decoupling the temperatures of the jets when fitting the data, we made sure that the difference in their values did not exceed 2 keV. The approximation introduced in this way becomes necessary when considering a continuum with a neutral iron absorption edge (see Section 4.5), because the photoabsorbed flux can be compensated by an increase in the temperature of the red jet and, as a consequence, the flux of the Ni XXVIII Ly_α line of the red jet. In this case, the flux of the Fe I K_α line decreases, while the temperature of the red jet becomes considerably higher than that of the blue one. It is obvious from general considerations about the system's geometry that the range of such parameters is physically ungrounded.

The line widths are specified by convolving the `lbjet` model with a Gaussian function with a width $\Sigma_{E0} = \Sigma_{\rm jet} \times (E_0/6\ {\rm keV})$. The Doppler shift of the blue and red jet lines, as before, is defined by the parameters z_b and z_r. The fluorescent Fe I K_α and Ni I K_α lines are described by narrow Gaussians with widths $\Sigma_{\rm Ni\,I} = \Sigma_{\rm Fe\,I} = 5$ eV. In addition, similarly to the previous model, we will add a narrow Gaussian with a width $\Sigma < 5$ eV and a centroid near 6.6 keV. The total number of free model parameters is 13.

The derived best-fit parameters are presented in Table 2. An important advantage of the `lbjet` model over the phenomenological model is the possibility of constraining the relative fluxes of weak lines using the temperature alone; therefore, we no longer need to use the assumptions described in Section 4.2. As can be seen from the derived constraints on the Ni I K_α line flux, the contribution of the red jet lines disregarded in the phenomenological model, mostly Ni XXVIII Ly_α and the weaker lines of the K-series (β, γ, δ...) of helium-like iron,[9] turns out to be important when fitting the spectral region near 7.5 keV.

The width of the jet lines was found to be $\Sigma_{\rm jet} = 63^{65}_{61}$ eV, which is more than twice the value inferred from the soft part 1–3 keV of the standard X-ray band by analyzing the Chandra data ($\Sigma_{\rm jet} \sim 30$ eV, Marshall et al. 2002; Khabibullin et al. 2016) and expected for a jet opening angle of $\sim 1.5°$. On the one hand, broader jet lines are actually observed in the hard part of the spectrum 6–9 keV. For example, for the Fe XXV K_α triplet Namiki et al. (2003) measured $\Sigma_{E0} \sim 50$ eV (based on HETGS/Chandra data). On the other hand, the width being determined can be affected by the instrumental response, because the EPIC-pn camera has a relatively low spectral resolution, $\Delta E_{FWHM} \gtrsim 2.36\Sigma_{\rm jet}$. In addition, the inferred large line width $\Sigma_{\rm jet}$ may point to a spectral

[9] The satellites of bright lines can also make a noticeable contribution (for more details, see Khabibullin et al. 2016).

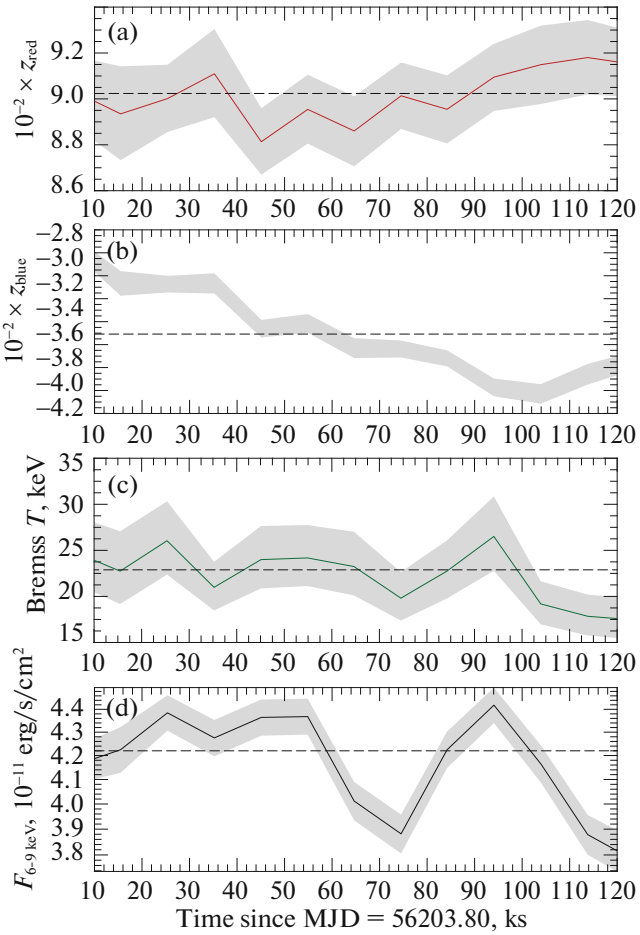

Fig. 9. (Color online) Spectral variability of SS 433 within the total 120-ks exposure of the XMM-Newton observation. The total exposure was divided into 12 10-ks-long parts in each of which the continuum was described by the bremsstrahlung model in the spectral regions 4.3–5.8 and 10–12 keV containing no bright lines. The two upper panels show the Doppler shifts of the blue, z_b, and red, z_r, jets determined when fitting the data by the `lbjet` model in the energy range 4.3–12 keV. The lower panels show the evolution of the continuum parameters: the bremsstrahlung temperature and the 6–9 keV flux. The gray band corresponds to a 90% confidence level. The dashed horizontal lines indicate the parameters found by analyzing the total exposure.

variability of the source within the total exposure, as a result of which the line profile is poorly described by a Gaussian function.

4.4. Evolution of the Spectrum Within the Total Exposure

It can be seen from the light curves (Fig. 2) that the flux in the hard part of the standard X-ray band has a noticeable variability on the time scale of the total exposure. In addition, the spectral evolution of the source turns out to be also significant. We investigated the spectral variability by dividing the total 120-ks exposure into 12 10-ks-long parts.

The two upper panels in Fig. 9 show the Doppler shifts of the red and blue jet lines obtained by analyzing the individual 10-ks spectra using the `lbjet` model. The lower panels present the corresponding parameters of the continuum model. The quality of the continuum fit averaged over 12 spectra corresponds to $\chi^2/\text{d.o.f} = 700/696 = 1.006$ (recall that we use unbinned spectra).

The average rate of change in the positions of the blue jet lines over the total exposure time is $\Delta z_b/\Delta t = 0.99^{1.11}_{0.85} \times 10^{-2}$ day^{-1}. The sharpest jump in the positions of the blue jet lines on a time scale of 10 ks was found to be $\Delta z_b \approx 0.4 \times 10^{-2}$, which corresponds to $\max(dz_b/dt) = 3.45^{4.89}_{2.01} \times 10^{-2}$ day^{-1}. At the same time, the expected maximum variability due to the sinusoidal nutational motions of the jets with a period of 6.3 days is $dz/dt \approx 1.21 \times 10^{-2}$ day^{-1} (Fabrika 2004). Thus, the average change in the line positions on a time scale of ~100 ks is consistent with the nutational–precessional variability of the system, while the sharp jumps of the lines in a time of ~10 ks

Table 2. Parameters of the best fit by the `lbjet` model to the 120-ks XMM-Newton EPIC-pn spectrum of SS 433 in the energy ranges 4.3–6.58 and 6.72–12 keV

lbjet parameter	Blue jet	Red jet
T_0, keV	$12.3^{12.6}_{11.9}$	$= T_{0,b}$
$Z_{\rm Ni}/Z$	$8.9^{9.3}_{8.7}$	$= (Z_{\rm Ni}/Z)_b$
$n = \tau_{e0} \times L_k^{\rm a}$	$3.72^{3.76}_{3.66}$	$1.80^{1.83}_{1.77}$
$z \times 10^{-2}$	$-3.51^{-3.49}_{-3.53}$	$8.98^{9.03}_{8.93}$
$\Sigma_{\rm jet}$, eV	63^{65}_{61}	$= \Sigma_{{\rm jet},b}$
Spectr. symbol	Fluorescent lines	
	E_0, keV	Flux (eq. width), 10^{-4} phot s^{-1} cm^{-2} (eV)
Fe I K$_\alpha$	$6.449^{6.456}_{6.440}$	$0.96^{1.00}_{0.94}$ (46^{48}_{44})
Ni I K$_\alpha$	$7.5^{7.5}_{7.5}$	$0.00^{0.01}_{0.00}$ ($0.0^{0.9}_{0.0}$)
Fe (XXII–XXIII K$_\alpha$?)	$6.63^{6.64}_{6.62}$	$0.97^{1.04}_{0.93}$(39^{41}_{36})

[a] $\times 10^{38}$ erg/s.

T_0 is the jet base temperature, $Z_{\rm Ni}/Z$ is the relative nickel overabundance in solar abundance units, and n is the line normalization parameter. The relative abundances $Z_{\rm Ni}/Z$ and the line widths $\Sigma_{\rm jet}$ for the red and blue jets are assumed to be equal. The unidentified line is denoted by Fe XXII–XXIII K$_\alpha$ (see Section 4.2). The quality of the fit corresponds to χ^2/d.o.f = 2231/1528 = 1.46.

Table 3. Fluxes of the fluorescent Ni I K$_\alpha$ and Fe I K$_\alpha$ lines, their ratio $R_{\rm fluor}$, the relative nickel overabundance in the SS 433 jets $Z_{\rm Ni}/Z$, and the ratio of the nickel abundances in the wind and the jets of SS 433 $Z_{\rm Ni,\,wind}/Z_{\rm Ni,\,jet}$ found by two methods: using the phenomenological model and when fitting the data by the `lbjet` model

Parameter	Phenomenological model	`lbjet`
F(Fe I K$_\alpha$), 10^{-4} phot s^{-1} cm^{-2}	$1.11^{1.13}_{0.96}$	$0.99^{1.12}_{0.84}$
F(Ni I K$_\alpha$), 10^{-4} phot s^{-1} cm^{-2}	$0.21^{0.35}_{0.07}$	$0.03^{0.09}_{0.00}$
$R_{\rm fluor}$,	$0.17^{0.29}_{0.05}$	$0.03^{0.10}_{0.00}$
$Z_{\rm Ni}/Z$	$8.6^{12.3}_{5.8}$	$8.6^{10.3}_{7.3}$
$Z_{\rm Ni,\,wind}/Z_{\rm Ni,\,jet}$	$0.44^{0.64}_{0.16}$	$0.08^{0.24}_{0.00}$
χ^2/d.o.f	1544/1526	1566/1528

The total exposure was divided into 12 10-ks-long parts each of which was fitted separately in the energy range 4.3–12 keV by the continuum model *without* the neutral iron absorption edge described in Section 4.1. The presented parameters correspond to the average values found from the individual 10-ks spectra.

are observed much faster and can be associated with the "jitter" motions of the jets (see, e.g., Iijima 1993; Kubota et al. 2010). If we now assume that the line width due to the transverse expansion of the jets is $\Sigma_\Theta \approx 30 \times (E_0/6\ {\rm keV})$ eV, then we can estimate the line broadening due to the jitter:

$$\Sigma \approx \sqrt{\Sigma_\Theta^2 + (\delta E_0/2\sqrt{3})^2}, \qquad (3)$$

where $\delta E_0 = \frac{E_0}{(1+z)^2}\Delta z$ is the motion of the line centroid within the 10-ks exposure. For the Fe XXV K$_\alpha$ 6.4 keV line of the blue jet and $\max(\Delta z_b) = 0.39 \times 10^{-2}$ we obtain $\delta E_{0,{\rm Fe\,XXV\,K}\alpha} = 26.9$ eV. In that case, the line broadening due to the jitter should not be more than 5% of the width Σ_Θ. At the same time, the line width averaged over 12 parts is $\Sigma_{\rm jet} = 53^{59}_{47}$ eV, which is consistent with the results of Namiki et al. (2003) within the error limits.

To exclude the possible errors related to the source's spectral variability, we repeat the fitting procedure for each 10-ks spectrum separately using the two methods described above, i.e., the phenomenological approach and the `lbjet` model. Table 3 presents the results for the fluxes in the fluorescent lines and the relative nickel overabundance $Z_{\rm Ni}/Z$ in the SS 433 jets. Within the phenomenological approach we found the nickel abundance $Z_{\rm Ni}/Z$ from the flux ratio of the brightest nickel and iron lines in the spectrum: $R_{\rm jet} = F$(Ni XXVII K$_\alpha$)/F(Fe XXVII K$_\alpha$). In Fig. 10 this quantity is indicated by the blue horizontal line (the blue region corresponds to a 90% confidence level). We also calculated $R_{\rm jet}$ using the `lbjet` jet emission model for the entire range of parameters τ_{e0} from 5×10^{-5} to 0.5 and T_0 from 7 to 40 keV, which corresponds to the range of α from 10^{-4} to 10; the values obtained are indicated in Fig. 10 by the gray region (see also Fig. 6 in Khabibullin et al. (2016)). The value of $Z_{\rm Ni}/Z$ presented in Table 3 for the phenomenological model corresponds to the intersection of the blue and gray regions. The parameter of the best fit $Z_{\rm Ni}/Z$ to the spectra by the `lbjet` model is indicated in Fig. 10 by the red vertical line (the orange region is a 90% confidence level). The relative nickel abundances found by the two methods, on the whole, agree well between themselves (in average value). This serves as an additional argument for the adequacy of the fit to the data by the `lbjet` model, because the relative nickel abundance in this case depends not only on the

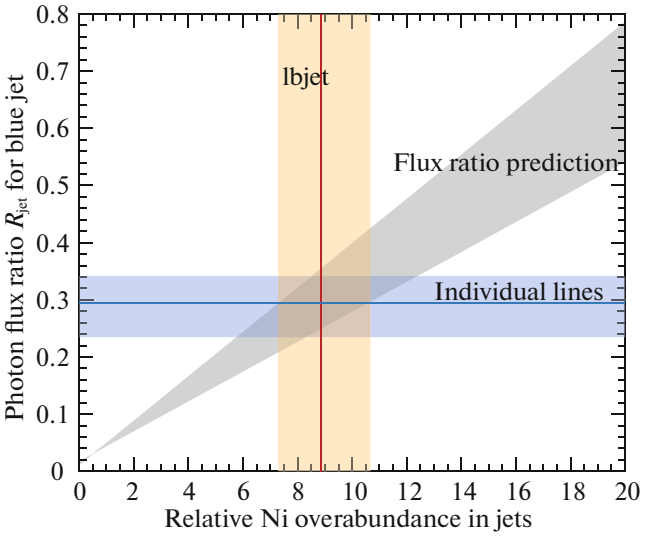

Fig. 10. (Color online) Relative nickel overabundance in the jets of SS 433 found from XMM-Newton data. The total 120-ks exposure was divided into 12 equal parts; the averaged best-fit parameters for each individual 10-ks spectrum are shown on the graph. The red line indicates the relative nickel overabundance $Z_{\rm Ni}/Z$ determined by fitting the data with the `lbjet` model. The blue line indicates the photon flux ratio in the K_α-triplets of helium-like nickel and iron $R_{\rm jet}$ obtained by fitting the data with the phenomenological model. The orange and blue regions indicate a 90% confidence level for $Z_{\rm Ni}/Z$ and $R_{\rm jet}$, respectively. The gray region corresponds to the prediction of this ratio from the `lbjet` model of the SS 433 jets, the scatter of values is attributable to the dependence of the line fluxes on other model parameters (mainly the temperature).

flux ratio $R_{\rm jet}$, but also on the jet temperature, which is determined by fitting all lines in the spectrum in the energy range under consideration.

It can be seen from Table 3 that, in addition to the overestimated value of $R_{\rm fluor}$ due to the contribution from the disregarded Ni XXVIII Ly_α line of the red jet described in the previous subsection, the phenomenological model gives a large spread in $Z_{\rm Ni}/Z$. This result is a consequence of the large range of possible values for the parameter $Z_{\rm Ni}/Z$ at a fixed flux ratio $R_{\rm jet}$ (the gray region in Fig. 10).

4.5. The Neutral Iron Absorption Edge

In the final step, we investigate the influence of the neutral iron absorption edge on the flux ratio $R_{\rm fluor} = F({\rm Ni\ I\ K}_\alpha)/F({\rm Fe\ I\ K}_\alpha)$. For this purpose, we describe the continuum with the absorption edge as follows:

$$I(E) = \begin{cases} I_{ff}(E), & E \leqslant E_{\rm edge} \\ I_{\rm edge}(E) I_{ff}(E), & E > E_{\rm edge}, \end{cases} \quad (4)$$

where $I_{ff}(E)$ is the bremsstrahlung spectrum, $E_{\rm edge} = 7.1$ keV is the position of the absorption edge, and $I_{\rm edge}(E) = \widetilde{N} \exp[-\tau_{\rm edge}(\frac{E}{E_{\rm edge}})^{-3}]$ is the absorption edge model parameterized by two quantities: $\tau_{\rm edge}$ is the optical depth for photoabsorption at the energy $E_{\rm edge}$ and $\widetilde{N}$ is the normalization parameter that specifies the fraction of the absorbed flux on the line of sight. As follows from Section 3, the shape and depth of the absorption edge depend on the geometry and optical depth of the reflecting/scattering medium. To span the entire range of possible scenarios, we define the parameter $\widetilde{N}$ via the flux in the fluorescent Fe I K_α line in such a way that the following equality holds:

$$N_{\rm edge} F({\rm Fe\ I\ K}_\alpha) \quad (5)$$
$$= \int_{E_{\rm edge}}^{\infty} [I_{ff}(E) - I_{\rm edge}(E) I_{ff}(E)] dE,$$

where $N_{\rm edge}$ is a model parameter.

We consider the optical depth at the absorption edge $\tau_{\rm edge}$ as a free model parameter. We estimate the upper limit on this parameter by assuming the neutral iron photoabsorption cross section at the absorption edge energy to be $\sigma_{\rm Fe\,I} = 3.764 \times 10^{-20}$ cm^2 (the `XCOM` database[10]). The ratio of the optical depth for neutral iron photoabsorption to the optical depth for electron scattering on the line of sight can then be estimated as

$$\left.\frac{\tau_{\rm ph.abs}}{\tau_e}\right|_{E=7.1{\rm keV}} \sim \frac{n_{\rm Fe}}{n_e}\frac{\sigma_{\rm Fe\,I}}{\sigma_e} \approx 2.2 \quad (6)$$

for the solar chemical composition of the gas (Anders and Grevesse 1989). Therefore, as a conservative estimate we set the upper limit on this parameter equal to $\max(\tau_{\rm edge}) = 2$.

In view of the relatively poor spectral resolution of the EPIC-pn instrument, the parameter $N_{\rm edge}$ is difficult to constrain from the observed spectrum. When fitting the data by the model with the continuum specified by Eq. (4), the parameter $N_{\rm edge}$ has a significant degeneracy. As a result, the errors in the model parameters determined by analyzing the data turn out to be overestimated (for more details, see the Appendix and the marginalized distributions in Fig. 12). To avoid a large scatter of parameters, we fix $N_{\rm edge}$ on a grid of values for each of which we apply the fitting procedure described in the previous section.

The range of values for the parameter $N_{\rm edge}$ can be estimated using the two models presented in Section 3: `pexmon` and `cwind`. For this purpose, we

[10] https://www.nist.gov/pml/xcom-photon-cross-sections-database

fitted the continuum of the emergent radiation in the models by a smooth function in the spectral ranges unaffected by the absorption edge and containing no fluorescent lines. Thereafter, by subtracting the photon flux predicted in the model with the absorption edge from the photon flux above 7.1 keV calculated from the approximation model, we effectively find the value corresponding to the normalization $\widetilde{N}$. The predicted photon flux in the 6.4 keV line is determined similarly, which, as a result, allows us to calculate the relative normalization of the absorption edge $N_{\rm edge}$ that we use to analyze the spectra.

In the scenario for the formation of fluorescent lines when the radiation is reflected from an optically thick slab represented by the `pexmon` model, the parameter $N_{\rm edge}$ lies in the range 2–2.5 for inclination angles of the reflecting slab to the line of sight i from 5° to 90° (see also Basko 1978). In the case where the radiation passes through an optically thin cloud (`cwind` model), the parameter $N_{\rm edge}$ is determined almost exclusively by the geometry of the scattering region. For example, for a source places at the center of a spherically symmetric cloud ($\mu_d = 1$), the ratio of the Fe I K_α line flux to the K-edge absorbed flux is approximately equal to the fluorescent yield of iron ($\omega_K = 0.34$, Bambynek et al. 1972), which gives $N_{\rm edge} \approx 3$ (for more details, see Sunyaev and Churazov 1998). If, however, the column density of the scattering material along the line of sight is greater than that averaged over the angle around the source, then the emergent spectrum will be characterized by weak fluorescent lines. Therefore, for the line of sight perpendicular to the disk axis ($\mu = 0$), the parameter $N_{\rm edge}$ becomes larger with increasing opening angle $\Theta_d = \arccos\mu_d$, reaching $\sim$10 for $\Theta_d \approx 70°$. Note that for the simple geometry assumed in the `cwind` model the wind funnel opening angles $\Theta_d \gtrsim 60°$ are unlikely, because at precession phases of the system close to zero the angle between the line of sight and the accretion disk axis is 57° (Fabrika 2004) and, hence, the observer would look into the wind funnel. In that case, one might expect a much greater precessional variability of the system in the X-ray energy range. It is quite possible, however, that the physical picture of the formation of fluorescent lines may be much more complex, for example, as in the case of wind clumpiness or different degrees of gas ionization in the wind. In this paper we specify the range of $N_{\rm edge}$ from 0 to 10.

The dependence of the flux ratio $R_{\rm fluor}$ on the depth of the absorption edge $N_{\rm edge}$ is shown in Fig. 11. The derived parameters of the two models for $N_{\rm edge}$ at which the χ^2 statistic has the best value are given in Table 4. When the data are fitted with the phenomenological model, adding the absorption edge degrades the quality of the fit. The data fitting with the `lbjet` model is consistent with a larger depth of the absorption edge: the weak jet lines together contribute noticeably to the continuum in the energy range 7–9 keV, the best fit is obtained for $N_{\rm edge} = 5$. In addition to the Ni I K_α line flux, the relative nickel overabundance in the jets needed to describe the observed spectrum increases with increasing depth of the absorption edge. However, the variation of this parameter turns out to be appreciably smaller.

Table 4. Fluxes in the fluorescent Ni I K_α and Fe I K_α lines, their ratio $R_{\rm fluor}$, the relative nickel overabundance in the SS 433 jet $Z_{\rm Ni}/Z$, and the ratio of the nickel abundances in the wind and the jets of SS 433 $Z_{\rm Ni,\,wind}/Z_{\rm Ni,\,jet}$ found from XMM-Newton data for the continuum model with the neutral iron absorption edge at 7.1 keV

Parameter	Phenomenological model	`lbjet`
F(Fe I K_α), 10^{-4} phot s^{-1} cm^{-2}	$1.11^{1.13}_{0.96}$	$0.86^{1.11}_{0.72}$
F(Ni I K_α), 10^{-4} phot s^{-1} cm^{-2}	$0.21^{0.35}_{0.07}$	$0.11^{0.25}_{0.01}$
$R_{\rm fluor}$	$0.17^{0.29}_{0.05}$	$0.13^{0.21}_{0.01}$
$Z_{\rm Ni}/Z$	$8.6^{12.3}_{5.8}$	$10.1^{11.6}_{8.5}$
$Z_{\rm Ni,\,wind}/Z_{\rm Ni,\,jet}$	$0.44^{0.64}_{0.16}$	$0.28^{0.62}_{0.03}$
$N_{\rm edge}$	0	5
χ^2/d.o.f	1544/1526	1545/1528

The presented average parameters were determined from the individual 10-ks spectra using the phenomenological and `lbjet` models. The parameter $N_{\rm edge}$ specifies the depth of the absorption edge in units of the Fe I K_α line flux. The data were fitted for a grid of $N_{\rm edge}$ from 0 to 10. The presented results correspond to $N_{\rm edge}$ at which the model describes best the data in the energy range 4.3–12 keV.

5. DISCUSSION

The results of our analysis are presented in Tables 3 and 4 for the continuum models without and with the absorption edge specified by Eqs. (4) and (5), respectively. The phenomenological model has greater freedom in describing the data, because it allows the fluxes in the observed lines to be fitted independently. However, for the spectral resolution of the data used here such freedom is excessive, because we need to resort to additional constraints on the model parameters due to the blending of lines in the spectrum, which can be justified per se only based on the presumed physical picture of the formation of spectral lines. This is particularly true

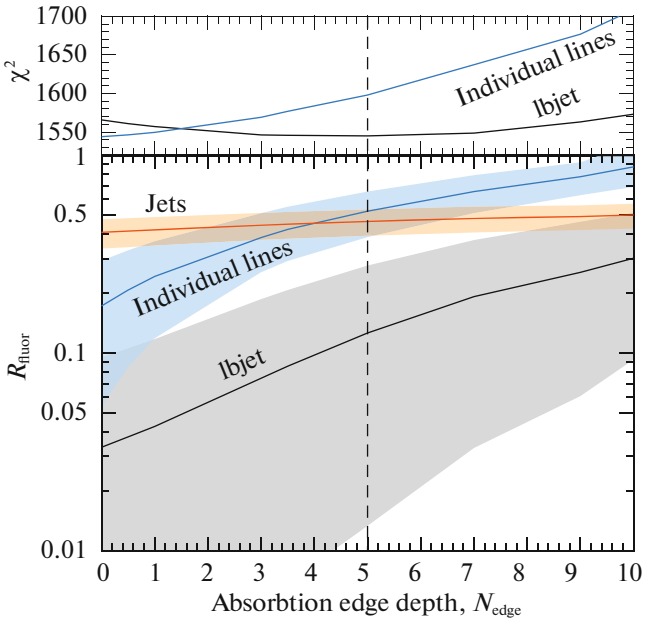

Fig. 11. (Color online) Bottom panel: ratio of the photon fluxes of the fluorescent Ni I K_α 7.5 keV and Fe I K_α 6.4 keV lines versus depth $N_{\rm edge}$ of the neutral iron absorption depth. The parameter $N_{\rm edge}$ specifies the fraction of the absorbed flux on the line of sight in units of the photon flux of the fluorescent Fe I K_α line (Eqs. (4) and (5)). The blue and black line indicate the flux ratio derived from the phenomenological model and determined within the spectral `lbjet` model, respectively. The shaded regions correspond to a 90% confidence level. The parameter $N_{\rm edge}$ is fixed on a grid of values from 0 to 10; the inferred parameters correspond to the values averaged over 12 spectra. The orange region corresponds to the predicted ratio $R_{\rm fluor}$ for the relative nickel abundance found for the jets by fitting the data with the `lbjet` model: $R_{\rm fluor} = 0.045 \times Z_{\rm Ni}/Z$ (see Section 3). Upper panel: the quality of the fit (χ^2) in the energy range 4.3–12 keV at different values of the parameter $N_{\rm edge}$. The blue and black lines indicate χ^2 for the phenomenological (d.o.f = 1526) and `lbjet` (d.o.f = 1528) models, respectively. The vertical dashed line indicates the parameter $N_{\rm edge}$ at which χ^2 has a minimum value when fitting the data with the `lbjet` model.

for relatively weak lines in the spectrum. In this case, the contribution of the Ni XXVIII Ly_α line, whose flux is expected to be 20% of the Fe XXVI Ly_α line flux for a relative nickel overabundance of ~10 (based on the jet emission model), i.e., $\sim 2 \times 10^{-5}$ phot s^{-1} cm^{-2} for the red jet, plays a fundamental role. This flux is very low in comparison with the flux in the iron lines of the blue jet, but is comparable to or higher than the expected flux in the fluorescent Ni I K_α line. For the precession phase of the system under consideration the centroid of the Ni XXVIII Ly_α line of the red jet falls at 7.41 keV, i.e., it is in the immediate vicinity of the line of interest. Hence, it can be concluded that the difference in $R_{\rm fluor}$ estimated by the two methods is related mainly to the contribution of the Ni XXVIII Ly_α line of the red jet, and, therefore, the parameters obtained for the `lbjet` model should be considered as the result of this study.

Assuming that the result obtained actually reflects the chemical composition of the SS 433 wind and jets, it can be supposed that much of the nickel observed in the jets should be synthesized in the immediate vicinity of the jet acceleration and collimation region. On the one hand, this assertion may be considered as an argument for a neutron star as the compact object in SS 433. In this sense, the *rp*-burning on the surface of a supercritically accreting neutron star (see, e.g., Schatz et al. 2001) seems the most natural mechanism capable of producing a large amount of nickel. On the other hand, this implies that the apparent nickel overabundance in the jets is attributable to the radioactive isotope nickel-56, which turns into radioactive cobalt 56 with a half-life of 6.1 days and then, with a half-life of 77.1 days, decays into stable iron-56 (see, e.g., Nadyozhin 1994). The emission lines associated with the decay ^{56}Co → ^{56}Fe were recorded in the observations of type Ia supernovae by the INTEGRAL gamma-ray observatory (Churazov et al. 2014).

At the same time, the radioactive decay of isotopes is accompanied by the release of energy in the form of gamma-ray photons with energies ~1 MeV. As a consequence, one might expect a stable flux in relatively narrow gamma-ray lines for the decay of nickel isotopes and significantly broader ones for the decay of cobalt-56 as a result of averaging over a time interval that is only half the precession period of the jets (162 days). The expected gamma-ray flux can be estimated by assuming the kinetic luminosity

of the jets to be $L_k \sim 3 \times 10^{39}$ erg s^{-1} (Khabibullin et al. 2016). The mass transfer rate in the jets will then be $\dot{M}_j = 1.6 \times 10^{-6}\ M_\odot$ yr^{-1}, which corresponds a rate of continuous injection and, hence, decay of nickel-56 isotopes at a level of 10^{39} nuclei per second. This, in turn, implies a line photon flux no more than $\sim 3.5 \times 10^{-7}$ phot s^{-1} cm^{-2} for both nickel and cobalt decay processes if the distance to SS 433 is assumed to be $\sim$5 kpc. Adding the fluxes from the two jets, we will get a photon flux $\lesssim 10^{-6}$ phot s^{-1} cm^{-2}.

Our flux estimate is at least two orders of magnitude smaller than the possible detection level of the INTEGRAL/SPI spectrometer (Winkler et al. 2003), the most sensitive instrument in the MeV range. At present, gamma-ray spectroscopy in this energy range runs into the problem of a high cosmic-ray background level. Therefore, detecting the predicted fluxes seems a promising and complex task for next-generation gamma-ray observatories, such as the planned e-ASTROGAM space mission with calorimeters (De Angelis et al. 2017).

6. CONCLUSIONS

In this paper we set an upper limit on the relative nickel abundance in the supercritical accretion disk wind of SS 433 based on the XMM-Newton X-ray data obtained on October 3–5, 2012. We selected this observation as best suited to the search for the fluorescent Ni I K_α line at 7.5 keV (Section 2).

In Section 3 we considered two models for the formation of fluorescent lines in the X-ray spectrum of SS 433: when the X-ray radiation is reflected from an optically thick neutral medium and in the case of radiation scattering by an optically thin gas followed by the emission of energy in fluorescent lines. The first case can correspond to the reflection of radiation from the hypothetical hidden central X-ray source of SS 433 off the walls of the supercritical disk wind funnel (Madvedev and Fabrika 2010). As a fit to the reflected spectrum emerging in this model we used the `pexmon` model (Nandra et al. 2007). In the second case, the hard component of SS 433 is the radiation from the hottest jet regions absorbed almost completely in the soft X-ray band, but only slightly modified in the hard X-ray band due to its passage through the region of the supercritical accretion disk wind that is optically thin for Thomson scattering, but optically thick for photoabsorption at energies below 3 keV. Since in this model the hard X-ray radiation is attenuated only slightly, there is no need for a bright central source. In such a situation the fluorescent Fe I K_α line observed in the spectrum of SS 433 emerges together with the scattered continuum. To fit the spectrum emerging in this case, we performed Monte Carlo simulations using the `cwind` spectral model (Churazov et al. 2017), which includes a complete calculation of the radiative transfer with Compton scattering, photoabsorption, and fluorescence by neutral atoms of the most abundant heavy elements. The main results of Section 3 are presented in Fig. 7; it shows the predicted flux ratio of the fluorescent iron and nickel lines $R_{\rm fluor} = F(\text{Ni I K}_\alpha)/F(\text{Fe I K}_\alpha)$. The value of $R_{\rm fluor}$ found lies in the range 0.45–0.5 for the relative nickel abundance $Z_{\rm Ni}/Z = 10$ and depends weakly on the model parameters. Using the `cwind` model, we checked that the ratio $R_{\rm fluor}$ is linearly scaled with the relative nickel abundance in the reflecting/scattering medium.

In Section 4 we placed a constraint on the fluorescent line flux ratio $R_{\rm fluor}$. We considered two methods of fitting the observed spectral lines: (1) using the phenomenological model that is the sum of individual bright lines described by Gaussians; (2) using the `lbjet` model of thermal X-ray radiation from the relativistic jets of SS 433 (Khabibullin et al. 2016) with the subtracted continuum described in Section 3. Since there is still no clear understanding of the processes responsible for the continuum formation in the spectral range under consideration, the continuum shape and level were determined in the spectral regions containing no bright lines: 4.3–5.8 and 10–12 keV. Both approaches give a similar result for the brightest spectral lines. However, the contribution of the red jet emission lines, whose relative brightness cannot be constrained within the phenomenological model due to the mutual overlapping (blending) of spectral lines, turns out to be important for constraining the flux of the weak Ni I K_α line. Therefore, the method of data fitting with the `lbjet` model was chosen as the main one.

A significant X-ray variability of SS 433 was detected during the XMM-Newton observation. Therefore, the total exposure was divided into 12 10-ks-long parts, which allowed us to exclude the influence of the source's spectral evolution on the estimate of the Ni I K_α line flux. The fluorescent line fluxes averaged over the individual 10-ks spectra were found to be $F(\text{Ni I}) = 0.03^{0.09}_{0.00} \times 10^{-5}$ phot s^{-1} cm^{-2} and $F(\text{Fe I}) = 0.99^{1.12}_{0.84} \times 10^{-4}$ phot s^{-1} cm^{-2} for the continuum specified by the bremsstrahlung model without the neutral iron absorption edge (see Table 3).

In the final step, we investigated the influence of the neutral iron absorption edge at 7.1 keV on the Ni I K_α line flux. For this purpose, we parameterized the absorption edge model using the ratio of the absorbed flux on the line of sight to the photon flux of the fluorescent Fe I K_α line (parameter $N_{\rm edge}$, Eqs. (4) and (5)). Repeating the data fitting procedure for a given parameter $N_{\rm edge}$ on a grid of

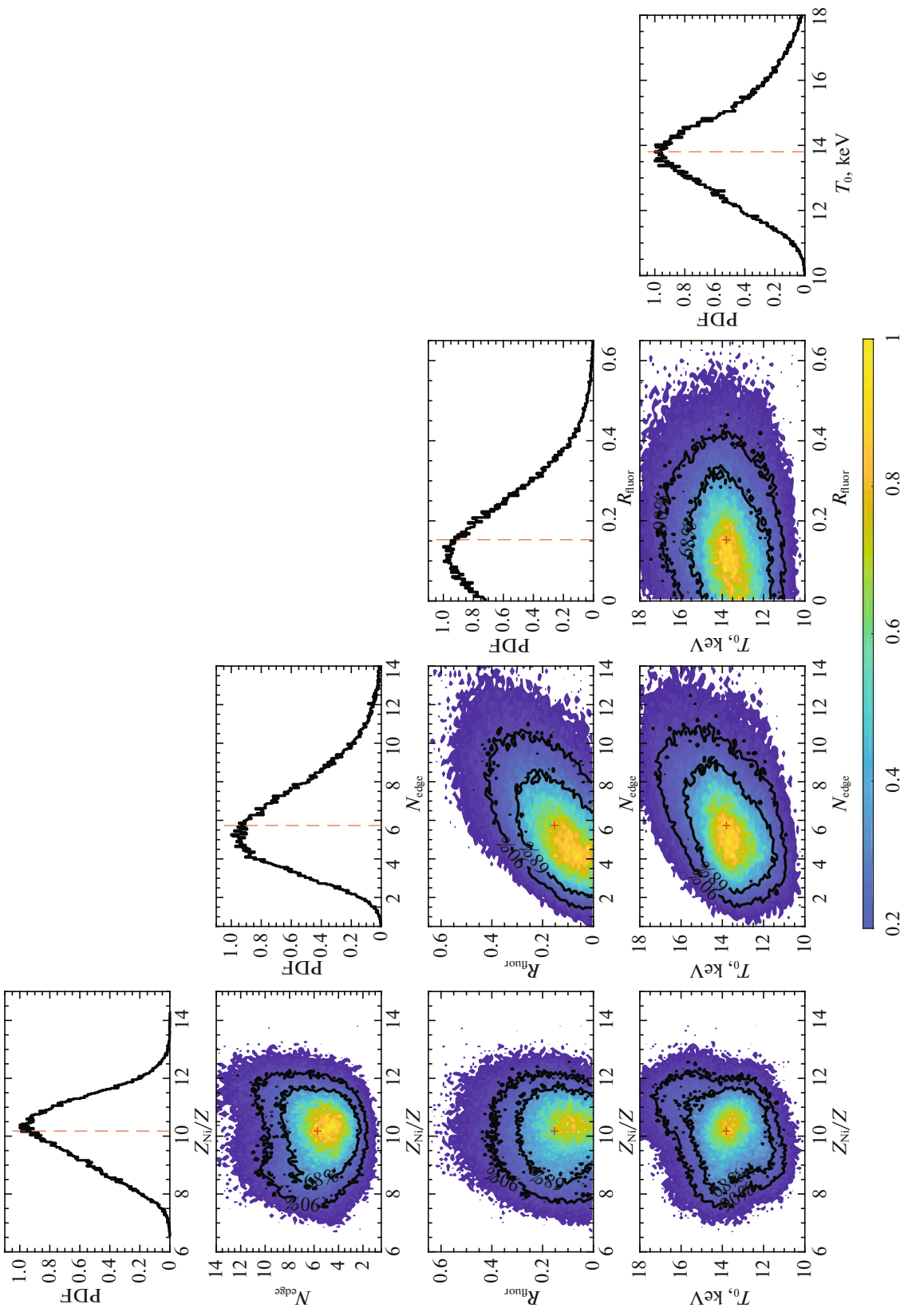

Fig. 12. (Color online) The one- and two-dimensional marginalized a posteriori distributions of `1bjet` model parameters obtained by fitting the data in the energy range 4.3–12 keV by the sum of the model and the continuum specified by Eqs. (4) and (5). These distributions were grouped from the distributions of parameters for the individual 10-ks spectra. The vertical dashed lines and red crosses indicate the median mean values of the parameters. The black contours in the two-dimensional distributions indicate 90 and 68% probability regions of the parameters. The color scale associates the color gamut of the distributions with the probability density of the parameters.

values from 0 to 10, we achieved the best agreement between the model and the data for $N_{\rm edge} = 5$. In this case, the fluorescent line fluxes were found to be $F(\text{Ni I}) = 0.11^{0.01}_{0.25} \times 10^{-5}$ phot s^{-1} cm^{-2} and $F(\text{Fe I}) = 0.86^{1.11}_{0.72} \times 10^{-4}$ phot s^{-1} cm^{-2} (see Table 4).

At the same time, the relative nickel abundance in the SS 433 jets was determined to be $Z_{\rm Ni}/Z = 10.1^{11.6}_{8.5}$. Based on the foregoing discussion, we conclude that the relative nickel abundance in the SS 433 wind should be much smaller than the observed nickel abundance in the jets: $Z_{\rm Ni,\,wind}/Z_{\rm Ni,\,jet} = 0.08^{0.24}_{0.00}$ for the continuum model with the absorption edge and $Z_{\rm Ni,\,wind}/Z_{\rm Ni,\,jet} = 0.28^{0.62}_{0.03}$ for the continuum model without the absorption edge.

APPENDIX

THE TECHNIQUE OF DATA ANALYSIS

We analyzed the observational data with standard tools from the XSPEC software package (version 12.9.1m, Arnaud 1996). For all of the models described here we applied the *wabs* multiplicative model of interstellar absorption with an atomic hydrogen column density $n_H = 1.2 \times 10^{22}$ cm^{-2} (Khabibullin et al. 2016). The *bremss* single-temperature bremsstrahlung model was used to describe the continuum. The Doppler shifts of the spectral lines were specified by the *zashift* tool. The spectral lines of the `lbjet` model were convolved with a Gaussian function using the *gsmooth* tool. To describe the neutral iron absorption edge, we adapted the *edge* model.

Since here we analyzed unbinned spectra, we used the statistical weighting method proposed by Churazov et al. (1996) to estimate the data variance within each channel. We also made sure that an analysis of the data binned by 25 counts per energy channel gives coincident results within the error limits.

The reliability of the result obtained and the degree of degeneracy of the individual model parameters were determined by the Markov Chain Monte Carlo (MCMC) method. The Metropolis–Hastings (Hastings 1970) algorithm was chosen as a Markov chain scheme. The initial parameters of the Markov chain were generated based on the covariance matrix of the best-fit model obtained by the method described in Section 4. This covariance matrix was first multiplied by 0.2 in order that the random walks of the chain cover better the model parameter space. Therefore, it is important to discard a sufficient number of initial steps $N_{\rm burn}$ for the derived a posteriori distributions of parameters to fall into the region of the greatest probability. We specify the parameter $N_{\rm burn}$ in the range from 10^4 to 5×10^4 steps by checking that this number is indeed sufficient for the Markov chain to reach a stable χ^2 distribution. The constraints on the model parameters represented here by the subscripts and superscripts, including those on the line fluxes, correspond to the ranges covering the parameters with a given a posteriori probability; in this paper we everywhere use the intervals between 5 and 95% quantiles (90% confidence level). The mean value of the parameters was determined as the average over the a posteriori distribution. When analyzing the 10-ks spectra, the final values of the model parameters, including the flux ratio of the Ni I K_α and Fe I K_α lines, $Z_{\rm Ni}/Z$, were determined from the distributions grouped from the a posteriori distributions for the individual 10-ks spectra.

In Section 4.5 we discussed the influence of the neutral iron absorption edge on the derived nest-fit parameters: the flux ratio of the fluorescent lines and the relative nickel abundance in the jets. In addition to the technique described in this section, whereby the depth of the absorption edge expressed in units of the fluorescent Fe I K_α line was specified on a grid of $N_{\rm edge} = 0{-}10$, we analyzed the data using similar models, but considering $N_{\rm edge}$ as a free model parameter. In this case, the continuum parameters, i.e., the bremsstrahlung temperature and normalization, are fitted together with the spectral lines in the energy range 4.2–12 keV. Figure 12 shows the one- and two-dimensional marginalized a posteriori distributions of `lbjet` model parameters: the relative nickel abundance $Z_{\rm Ni}/Z$, the absorption edge depth $N_{\rm edge}$, the fluorescent line flux ratio $R_{\rm fluor}$, and the jet temperature $T_0 = T_{0,b} = T_{0,r}$ (assumed to be equal in the fitting). The final distributions of parameters were obtained by grouping the distributions for the individual 10-ks spectra. The quality of the fit for the mean values of the parameters corresponds to $\chi^2/\text{d.o.f} = 1523/1524$. Because of the high degeneracy of $N_{\rm edge}$, the two-dimensional distributions have a shape elongated along this parameter. The derived mean values of the parameters are: $T_{0,b} = T_{0,r} = 13.9^{16.42}_{11.7}$ keV, $T_{\rm bremss} = 27.3^{40.5}_{18.2}$ keV, $N_{\rm edge} = 5.7^{10.2}_{2.7}$, $F(\text{Fe I K}_\alpha) = 0.8^{1.2}_{0.6} \times 10^{-4}$ phot s^{-1} cm^{-2}, $F(\text{Ni I K}_\alpha) = 0.139^{0.296}_{0.016} \times 10^{-4}$ phot s^{-1} cm^{-2}, $R_{\rm fluor} = 0.17^{0.39}_{0.02}$, $Z_{\rm Ni}/Z = 10.1^{11.8}_{8.2}$, and $Z_{\rm Ni,\,wind}/Z_{\rm Ni,\,jet} = 0.37^{0.85}_{0.04}$. The continuum bremsstrahlung temperature becomes higher with increasing absorption edge depth; therefore, the parameter $T_{\rm bremss}$ turns out to be poorly constrained.

ACKNOWLEDGMENTS

This was was supported by the Russian Science Foundation (project no. 14-12-01315).

REFERENCES

1. G. O. Abell and B. Margo, Nature (London, U.K.) **279**, 701 (1979).
2. E. Anders and N. Grevesse, Geochim. Cosmochim. Acta **53**, 197 (1989).
3. A. de Angelis, V. Tatischeff, I. A. Grenier, J. McEnery, M. Mallamaci, M. Tavani, U. Oberlack, L. Hanlon, et al., arXiv:1711.01265 (2017).
4. K. Arnaud, ASP Conf. **101**, 17 (1996).
5. W. Bambynek, B. Craseman, R. W. Fink, H. U. Freund, H. Mark, C. D. Swift, R. E. Price, and P. V. Rao, Rev. Mod. Phys. **44**, 716 (1972).
6. M. M. Basko, Astrophys. J. **223**, 268B (1978).
7. M. C. Begelman, A. R. King, and J. E. Pringle, Mon. Not. R. Astron. Soc. **370**, 399 (2006).
8. W. Brinkmann, B. Aschenbach, and N. Kawai, Astron. Astrophys. **312**, 306 (1996).
9. W. Brinkmann, H. H. Fink, S. Massaglia, G. Bodo, and A. Ferrari, Astron. Astrophys. **196**, 313 (1998).
10. W. Brinkmann, T. Kotani, and N. Kawai, Astron. Astrophys. **431**, 575 (2005).
11. A. M. Cherepashchuk, R. A. Sunyaev, K. A. Postnov, E. A. Antokhina, and S. V. Molkov, Mon. Not. R. Astron. Soc. **397**, 479 (2009).
12. E. Churazov, M. Gilfanov, W. Forman, and C. Jones, Astrophys. J. **471**, 673 (1996).
13. E. Churazov, R. Sunyaev, J. Isern, J. Knödlseder, P. Jean, F. Lebrun, N. Chugai, S. Grebenev, E. Bravo, S. Sazonov, and M. Renaud, Nature (London, U.K.)**512**, 406 (2014).
14. E. Churazov, I. Khabibullin, G. Ponti, and R. Sunyaev, Mon. Not. R. Astron. Soc. **468**, 165 (2017).
15. A. C. Fabian and M. J. Rees, Mon. Not. R. Astron. Soc. **187**, 13P (1979).
16. S. Fabrika, Astrophys. Space Phys. Rev. **12**, 1 (2004).
17. R. Fender and E. Gallo, Space Sci. Rev. **183**, 323 (2014).
18. E. Filippova, M. Revnivtsev, S. Fabrika, K. Postnov, and E. Seifina, Astron. Astrophys. **460**, 125 (2006).
19. A. R. Foster, L. Ji, R. K. Smith, and N. S. Brickhouse, Astrophys. J. **756**, 128 (2012).
20. Y. Fukazawa, S. Furui, K. Hayashi, M. Ohno, K. Hiragi, and H. Noda, Astrophys. J. **821**, 15 (2016).
21. I. M. George and A. C. Fabian, Mon. Not. R. Astron. Soc. **249**, 352 (1991).
22. V. Goranskij, Perem. Zvezdy **31**, 5 (2011).
23. W. K. Hastings, Biometrika **57**, 97, 109 (1970).
24. T. Iijima, Astrophys. J. **410**, 295 (1993).
25. J. S. Kaastra and R. Mewe, Astron. Astrophys. Suppl. Ser. **97**, 443 (1993).
26. T. R. Kallman, P. Palmeri, M. A. Bautista, C. Mendoza, and J. H. Krolik, Astrophys. J. Suppl. Ser. **155**, 675 (2004).
27. I. I. Khabibullin and S. Y. Sazonov, Astron. Lett. **38**, 443 (2012).
28. I. Khabibullin and S. Sazonov, Mon. Not. R. Astron. Soc. **457**, 3963 (2016).
29. I. Khabibullin, P. Medvedev, and S. Sazonov, Mon. Not. R. Astron. Soc. **455**, 1414 (2016).
30. T. Kotani, N. Kawai, M. Matsuoka, and W. Brinkmann, Publ. Astron. Soc. Jpn. **48**, 619 (1996).
31. Y. M. Krivosheyev, G. S. Bisnovatyi-Kogan, A. M. Cherepashchuk, and K. A. Postnov, Mon. Not. R. Astron. Soc. **394**, 1674 (2009).
32. K. Kubota, Y. Ueda, N. Kawai, T. Kotani, M. Namiki, K. Kinugasa, Sh. Ozaki, T. Iijima, et al., Publ. Astron. Soc. Jpn. **62**, 323 (2010).
33. L. A. Lopez, H. L. Marshall, C. R. Canizares, N. S. Schulz, and J. F. Kane, Astrophys. J. **650**, 338 (2006).
34. H. L. Marshall, C. R. Canizares, and N. S. Schulz, Astrophys. J. **564**, 941 (2002).
35. A. Medvedev and S. Fabrika, Mon. Not. R. Astron. Soc. **402**, 479 (2010).
36. M. Milgrom, Astron. Astrophys. **76**, L3 (1979).
37. S. Molendi, S. Bianchi, and G. Matt, Mon. Not. R. Astron. Soc. **343**, L1 (2003).
38. D. K. Nadyozhin, Astrophys. J. Suppl. Ser. **92**, 527 (1994).
39. M. Namiki, N. Kawai, T. Kotani, and K. Makishima, Publ. Astron. Soc. Jpn. **55**, 281 (2003).
40. K. Nandra, P. M. O'Neill, I. M. George, and J. N. Reeves, Mon. Not. R. Astron. Soc. **382**, 194 (2007).
41. K. Ohsuga and S. Mineshige, Astrophys. J. **736**, 2 (2011).
42. J. Poutanen, G. Lipunova, S. Fabrika, A. G. Butkevich, and P. Abolmasov, Mon. Not. R. Astron. Soc. **377**, 1187 (2007).
43. S. Sazonov and R. Sunyaev, Astrophys. J. **543**, 28 (2000).
44. S. Sazonov, E. Churazov, and R. Krivonos, Mon. Not. R. Astron. Soc. **454**, 1202 (2015).
45. H. Schatz, A. Aprahamian, V. Barnard, L. Bildsten, A. Cumming, M. Ouellette, T. Rauscher, F.-K. Thielemann, and M. Wiescher, Phys. Rev. Lett. **86**, 3471 (2001).
46. N. I. Shakura and R. A. Sunyaev, Astron. Astrophys. **24**, 337 (1973).
47. R. Sunyaev and E. Churazov, Mon. Not. R. Astron. Soc. **297**, 1279 (1998).
48. C. Winkler, T.J.-L. Courvoisier, G. di Cocco, N. Gehrels, A. Giménez, S. Grebenev, W. Hermsen, J. M. Mas-Hesse, et al., Astron. Astrophys. **411**, L1 (2003).
49. T. Yaqoob and K. D. Murphy, Mon. Not. R. Astron. Soc. **412**, 1765 (2011).

Translated by V. Astakhov